공학박사학위논문

다공성 물질에서의 액체 흡수 역학

Hydrodynamics of liquid imbibition in porous media

2015 년 2 월

서울대학교 대학원

기계항공공학부

김 정 철

다공성 물질에서의 액체 흡수 역학

Hydrodynamics of liquid imbibition in porous media

지도교수 김 호 영

이 논문을 공학박사학위논문으로 제출함

2015 년 2 월

서울대학교 대학원
기계항공공학부
김 정 철

김정철의 박사학위논문을 인준함

2015 년 2 월

위 원 장 최해천 (인)
부 위 원 장 김 호 영 (인)
위 원 전 두 리 (인)
위 원 박 형 민 (인)
위 원 문 명 운 (인)

Hydrodynamics of liquid imbibition in porous media

Jungchul Kim

Department of Mechanical and Aerospace Engineering

Seoul National University

A thesis submitted for the degree of

Doctor of Philosophy

February 2015

Abstract

Hydrodynamics of liquid imbibition in porous media

Jungchul Kim
Department of Mechanical and Aerospace Engineering
The Graduate School
Seoul National University

Liquid imbibition in a porous structure is mundanely observed in our daily lives, including such phenomena as water absorption into a sponge, ink imbibition in fibrous paper, a water cleaning process by towel or tissue, etc. In this thesis, we combine experimental observation and theoretical analysis to understand the hydrodynamics of liquid imbibition in porous media. We start with relatively simple two-dimensional (2-D) flows on rough porous surfaces, and then increase the complexity of the structure to eventually understand flows in three-dimensional (3-D) multiscale porous media.

We first consider one of the most representative 2-D wicking flows, ink writing, i.e. liquid spreading into porous plates from moving point source. We use hydrophilic microtextured silicon wafers (superhydrophilic substrate) as model paper, capillary tubes as model pens, and various liquids as model inks. We start by focusing on liquid spreading when the source is stationary.

Balancing surface tension force and viscous shear force, scaling law of blot spreading with time is derived. We then concentrate on the behaviors of the liquid when the source moves in a constant speed. Employing a simplified schematics delineating the frontal liquid flow from the moving source, geometrical analysis is coupled with aforementioned force balance. The front profile predicted by the scaling analysis shows good agreement with experimental results. Also, considering volume conservation, the line thickness is quantified by parametric analysis and verified by experiments.

Next, we focus on the role of pore structure in the dynamics of liquid wicking on 2-D substrate. In experiments, we prepare arrays of pillars of varying height, pitches, diameter, and skewness. Through the macroscopic model, deducing average capillary force and resisting shear force, we derive a scaling law of the liquid propagation, which applies for wide range of structural conditions. Through the microscopic model, we approach the dynamics more rigorously by considering the local pressure drop between consecutive pillars. Separating the microscopic propagation by *climbing* and *sweeping*, we derive scaling laws of the spreading dynamics. Comparing results of the macroscopic model and microscopic model, we derive the validation limit of the scaling law of macroscopic model.

We then consider flows within the dual sized porous media, the simplest form of multi-porous media. The employed structure consists of parallel substrates with micropillar arrays, separated by a millimetric gap. The flow involves the bulk flow at the millimetric gap and the film flow in the micrometric pores above the bulk. The bulk flow between the superhydrophilic surfaces

shows identical behavior to what is observed on smooth substrates, meaning that the bulk flow is independent of the microstructures. The flow of the film emanating from the bulk is affected by the bulk in the beginning, but becomes independent of the bulk flow in the late stages. The entire flow regimes are investigated by scaling analysis and verified by experiments. Also, the moment of the film emanating from the bulk is quantitatively estimated by comparing the rising speeds of bulk and film.

Finally, we investigate the flows in porous material of practical importance, cellulose sponge, containing various sized pores. We construct a simple model, delineating unit structure of sponge pores by introducing *large void* and *wall pores* of the sponge. We first study the horizontal flow in sponge to understand the flow without gravitational effects. The horizontal liquid propagation distance is found to obey the Washburn's rule. We turn to the vertical flow, which shows different flow behaviors depending on the rise height. When the rise height is small so that the large void can be completely saturated, liquid flow behavior is identical to the horizontal flow. Whereas, when the rise height is so large that the large void is saturated but partially. The rise height grows like $t^{1/4}$ with t being time. This unusual phenomenon is caused by the non-uniformity of permeability, which is inversely proportional to the square of rise height. The scaling laws for the entire flow dynamics show good agreement with experimental results.

Keywords : Surface tension, Porous media, Capillary imbibition, Superhydrophilic surface
Student Number : 2009 - 20672

Contents

List of Figures

List of Tables

Chapter 1

Introduction

Most of the materials in earth consists of plenty of various sized pores, such as igneous rocks, sap of trees, or cellulose sponges. When these materials contact with chemically intimated liquids, the liquids infiltrate into the materials, which is referred to as *Capillary imbibition into porous media*. The flow is due to the surface tension, mutual interaction between liquid molecules at the interface. The molecular tension at the surface tends to minimize the total surface area for minimizing surface free energy, which generates negative pressure beneath the liquid surface. The negative pressure drives spontaneous capillary flows.

Natural and industrial processes associated with capillary impregnation abound, including an ink in paper, a dye in fabric, oil in a porous rock, water in soil, sap in xylem or a biofluid in cartilage. Capillary phenomena also play an important role in various fields of nano- and bio-technology. Nanoscale patterns on semiconductor wafers may stick together due to the surface tension of an evaporating rinsing solution, which is one of major problems deteriorating production yield. Many lab-on-a-chip systems rely on capillary forces to pump liquid into channels. For optimization, highly sophisticated prediction and systematic fluid mechanical approaches of the flow are required.

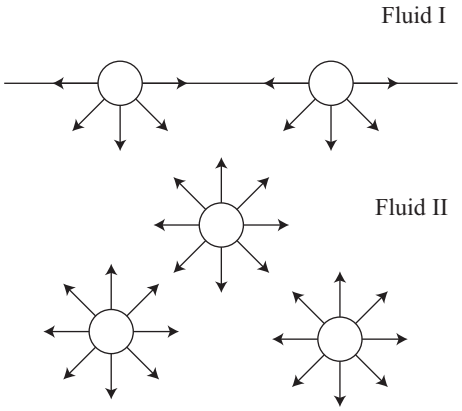

Figure 1.1: Schematic molecular structure of a fluid I - fluid II interface.

To understand the physics of the capillary flow, the fundamental characteristics of the liquid surface should be understood. When a fluid molecule is in the midst of the fluid, the molecule interacts with all other neighboring molecules, which is energetically favorable. However, when a fluid molecule is located at the interface, the molecule loses the interaction energy due to the part facing with the other fluid, which is energetically unfavorable. (See Fig. 1.1) The molecules tend to become the energy state of being perfectly neighbored with molecules of same fluid; thus, all of the fluid molecules minimize the exposed area, of which the force is characterized by interfacial tension coefficient. (N/m) The interfacial tension when the fluid is liquid faced with air is usually called by surface tension. (Butt *et al.*, 2006) For this reason, when a liquid drop is in the air, the drop tends to form a spherical shape.

Due to the surface tension, pressure difference between inside and outside of the surface arises. The magnitude of the pressure difference is estimated by the static force relation with the schematics in Fig. 1.2, which is equal to $\kappa\sigma$ with κ and σ being principal curvature and surface tension coefficient, respectively. When the liquid is faced with different material, the attraction between the liquid and the material significantly affects the

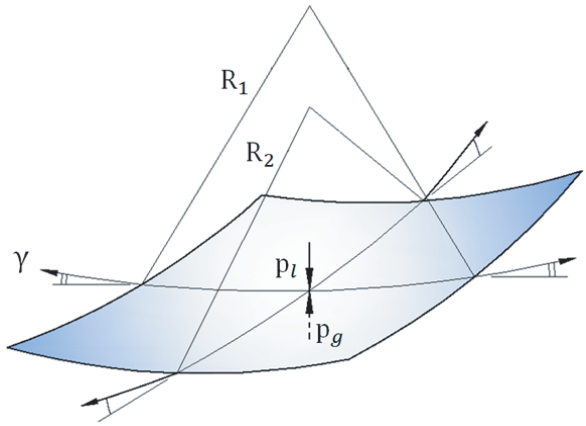

Figure 1.2: Normal pressure balance on an interface between gas and liquid. (Kovacevic, 20125)

shape of the surface. When the material is positively attractive to the liquid,(hydrophilic) liquid tends to face with the material more, which makes the contact angle smaller. In contrast, when the material is negatively attractive,(hydrophobic) the contact angle becomes larger. According to the contact angle, the local surface curvature is determined which eventually decides the magnitude of the pressure difference, which drives the capillary flows.

For understanding the fundamental physics of the capillary imbibition, the simplest form, capillary imbibition in two parallel plates or capillary tube has been intensively studied. (Duarte *et al.*, 1996; Popescu *et al.*, 2008; Washburn, 1921; Xiao *et al.*, 2006) As shown in Fig. 1.3, liquid spontaneously rises up though the cylindrical tube when the plate ends touch the liquid surface. In this case, surface tension of the liquid drives the flow, whereas gravity and the viscous shear force resist the flow. At the very beginning, inertial effect is dominant since the flow speed is quite high. In this case, the driving force, surface tension is balanced with the inertial force, which gives the speed, $\approx (2\sigma/(\rho r)^{1/2})$, with σ and r being surface

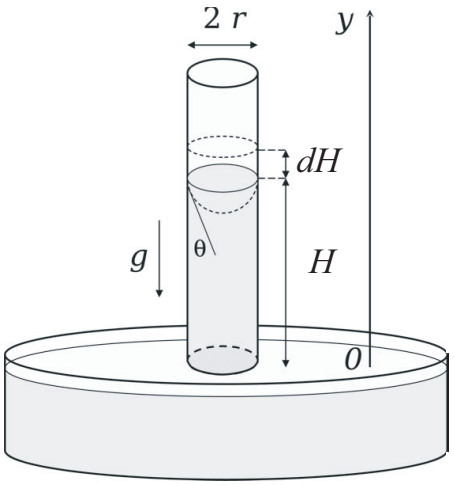

Figure 1.3: Schematic drawing of liquid rising along the capillary tube of radius r vertically inserted in the liquid bath. (Popescu *et al.*, 2008)

tension coefficient and tube radius, respectively. (Quéré, 1997) Due to the constant speed independent of the rise height, the flow dynamics shows linearity. However, for the common narrow long tube, the linear region is not largely formed. The size of the region is determined by considering the inertia and the viscous shear force. For the resisting force, the inertial force is dominant at the beginning, but the viscous shear force is eventually dominant at the late time. The boundary of these two regions is evaluated by balancing the two forces, which is scaled as $\sim \rho U r^2/\mu$, with U and μ being initial rise speed and viscosity, respectively. This length scale (L_e) is the entrance length which means the length required for the imbibed liquid fully developed. The time scale $\rho r^2/\mu$ means the time necessary for the viscous boundary layer to diffuse on the order of the radius of tube. (See Fig. 1.4(a)) However, the size of the entrance length is order of 10^-6 10^-5 m for the capillary tube, of which the radius is a few hundred microns, which is usually quite small value comparing with the capillary rise height, $O(10^-2)$m.

Apart from the entrance region, the velocity profile becomes parabolic,

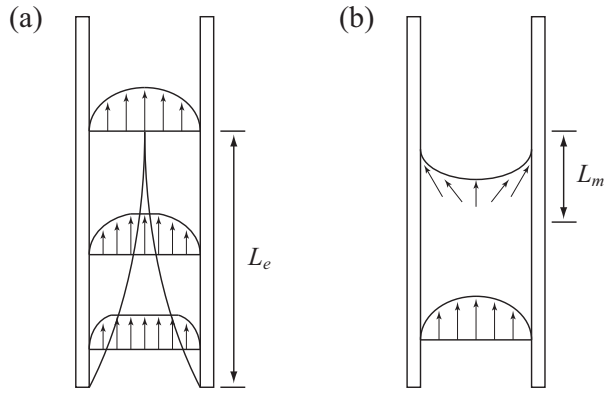

Figure 1.4: Schematics of velocity profiles (a) at the entrance region and (b) at the interface.(Zhmud *et al.*, 2000) Liquid split occurs beneath the meniscus.

which is significantly associated the shear stress. Considering the laminar flow for parallel plates and the Poiseuille flow for tube, the shear stress is written in the form of $k\mu U/r$ where k is a constant when we assume the no slip boundary condition. If the entrance region is relatively large, oscillation can occur.(Zhmud *et al.*, 2000) If the viscosity can be ignored, the overshoot trajectory points show parabolic shape where the oscillation is non-linear due to the variable mass. Quéré (1997).

Near the contact line, the parabolic velocity profile can not be sustained. (See Fig. 1.4(b)) The mechanism of the flow behavior near contact line has been studied mathematically. (Levine *et al.*, 1979) Moreover, flow field beneath the contact line has been observed by PIV technique, as shown in Fig. 1.5(a) and (b). (Fuentes & Cerro, 2005) However, theoretical approaches based on experiments are required for better understanding. The size of the region where the liquid split occurs is known to be a few radii, $L_m \sim O(r)$. Therefore, when the rise height is as much as H, the resisting force, shear stress times exerted area, is written as $\mu U(H - L_e - L_m)/r$. In most of cases of the capillary imbibition, the flow distance of the entire subjects is quite larger than the entrance length or the size of tube. So, the

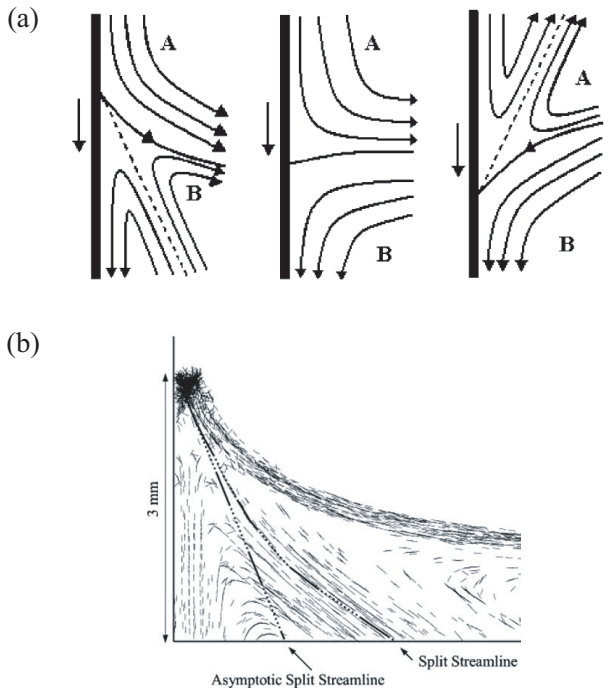

Figure 1.5: (a) Sketch of streamline patterns near the moving contact line during immersion of a solid surface into a pool of liquid. (b) View of flow field near moving contact line. (Fuentes & Cerro, 2005)

resisting shear force can be simply written as $\mu UH/r$.

Based on this fundamental studies of capillary imbibition, more practical researches for the more complicated flow in porous structures are performed for last decades. Uniformly arranged porous structures were used to alleviate the difficulties of irregularity of the actual porous structures.

For 2-D flow, a plate having uniform micro pillar arrays was used, which shows the most fundamental liquid flow behavior in porous structure (Courbin *et al.*, 2007; Ishino *et al.*, 2007; Kim *et al.*, 2011a,b). Due to the energetically stable state, the liquid flow is reported to show intrigue behavior, such as zipping in uniform pillar arrays. For 3-D flow, various sized glass beads were used to form tiny spaces where liquid flow occurs, espe-

cially in soil science (Delker *et al.*, 1996; Lago & Araujo, 2001). And corner flow within smooth substrate has been studied with introducing different scaling law, $x \sim t^{1/3}$ from the classical Washburn's dynamics ($x \propto t^{1/2}$) (Ponomarenko *et al.*, 2011; Weislogel, 2012).

However, in spite of the studies above, there remain a number of unanswered capillary-imbibition problems that occur in various fields of science and engineering. Major difficulties of understanding the dynamics of wicking come from the incomplete knowledge of formation and motion of three-phase (solid-liquid-fluid) contact lines. Furthermore, inherently complex geometry of pore structures in most porous media aggravates theoretical understanding and experimental measurements of wicking flows. As a result, more systematical theoretical approaches are demanded based on reasonable experimental results.

Here, we introduce four different subjects of capillary imbibition into porous media. At first, a representative classical example of the subject, "Physics of ink writing" is rationalized by our own theory. The behavior of the ink spreading from stationary and moving pen is mathematically quantified by parameters of properties of liquid and substrate, pen size, and moving speed. And, as the first step of the stepwise studies of the subject, we quantify the dynamics of hemiwicking more accurately and reveal the detailed meaning of the scaling analysis widely performed in this academic field. And, as the second step, liquid imbibition in dual sized porous system is studied as the simplest form of the multi porous structures, where correlation of flows in the two different sized pores is introduced. And, as the third step, an actual multi porous system, cellulose sponge has been employed for entire liquid behavior. Capillary rise within the pores of sponge has been quantified, associated with pores whose sizes are verified by pore size histogram. The studies above help us to understand overall liquid behaviors in porous media, experimentally and theoretically. We conclude with proposing a mundane but important problems, liquid flow

within a corner of porous plates and other flows associated with additional chemical effects such as swelling, which remain unanswered.

Chapter 2

Hydrodynamics of writing with ink

2.1 Introduction

For millenia, writing has been the preferred way to convey information and knowledge from one generation to another. We first developed the ability to write on clay tablets with a point, and then settled on a reed pen, as preserved from 3000 BC in Egypt when it was used with papyrus (Fischer, 2005). This device consisted of a hollow straw that served as an ink reservoir and allowed ink to flow to its tip by capillary action. A quill pen using a similar mechanism served as the instrument of choice for scholars in medieval times, while modern times have seen the evolution of variants of these early writing instruments to a nib pen, a ballpoint pen, and a roller ball pen. However, the fundamental action of the pen, to deliver liquid ink to an absorbent surface has remained unchanged for five thousand years.

2.2 Experimental setup

Although capillary imbibition on porous substrates has been studied for decades (Conrath *et al.*, 2010; Courbin *et al.*, 2007; Davis & Hocking, 2000; Ishino *et al.*, 2007; Washburn, 1921), how liquids spreads on a rough substrate (paper) from a moving source (pen), a basic process underlying ink writing, seems to not have been treated thus far. Writing with a given pen leaves a marked trail whose character is determined by the ink, the paper and the speed and style with which one moves the pen, and an example is shown in Fig. 2.1. To understand the characteristic hydrodynamics of this process, we employ a minimal system consisting of a straight capillary tube, our pen that is held in close proximity of a hydrophilic micropillar array, our porous paper (see Fig. 2.2), and moves parallel to it. The shape and size of the liquid trail that results is what we call writing, and arises as a consequence the quasi-two-dimensional hydrodynamic problem of capillary-induced spreading from a moving source.

The model pen is an open glass capillary tube (inner radius $R \in [0.25\ 1.00]$ mm, wall thickness 0.1 mm) filled with a liquid that is translated by a linear stage at a speed u_0, which varies in the range [0 3.0] mm/s while maintained constant in each experiment. The inner surface of the tube is cleaned with a piranha solution to have a nearly zero contact angle with all the liquids used here, while the outer surface is coated with PTFE (polytetrafluoroethylene), which is hydrophobic, to prevent the liquid from climbing onto the outside. Our model inks were aqueous glycerine solutions with different concentrations: 63 (liquid A), 73 (B) and 78.5 (C) wt% and ethylene glycol 99 wt% (D), whose physical properties are listed in Table 5.1. The model paper was a silicon wafer decorated with cylindrical micropillar arrays which are formed by the DRIE (deep reactive ion etching) process, and then additionally plasma-etched by O_2 to make them superhydrophilic (Yi *et al.*, 2010). The individual pillars are cylindrical (Fig. 2.2b) with height h and diameter d, and arranged in a square array with pitch s: $\{h, d, s\} \in [10\ 20]$

μm. The liquid from the tube starts to wick into the forest of pillars as the tube bottom gently touches the substrate, and a CCD (charge coupled device) camera (frame rate 30 s^{-1}) is used to image the spreading front.

	Liquid	γ (N/m)	μ (Pa·s)
A	Water	0.073	0.0013
B	Silicone oil	0.020	1.050
C	Glycerine 90 wt%	0.065	0.125
D	Ethylene Glycol 99 wt%	0.048	0.018

Table 2.1: Liquid properties at about 23°C.

2.3 Stationary pen

Placing a pen on paper before knowing what to write leads to a spreading stain that all of us have had some experience with. To understand the dynamics of the formation of this blot, we hold the pen fixed, and see a circular front emanating from it, as shown in Figs. 2.1(a) and 2.2(a). On these scales, fluid inertia is unimportant (Reynolds number based on the pillar height $\in [10^{-4} - 10^{-7}]$). The flow is driven by capillary forces at the spreading rim distant by r from the source, $F_{d,s}$, which can be obtained by considering the change of surface energy associated with the increase of a disk radius from r to $r+\mathrm{d}r$: $\mathrm{d}E = 2\pi r[\gamma(1-\frac{\pi}{4}d^2/s^2)+(f-\frac{\pi}{4}d^2/s^2)(\gamma_{SL}-\gamma_{SG})]\mathrm{d}r = -2\pi\gamma(f-1)r\mathrm{d}r$, where γ, γ_{SL} and γ_{SG} is the interfacial tension between liquid-gas, solid-liquid and solid-gas, respectively, and f is the roughness defined as the ratio of the actual solid surface area to the projected area. Here we used Young's equation, $\gamma\cos\psi = \gamma_{SG} - \gamma_{SL}$, where the contact angle $\psi \approx 0$.We note that the precursor film of the aqueous solutions may be present on the superhydrophilic surface, but the energy change associated with replacing solid-gas interface by solid-liquid interface and that

with covering the precursor liquid are the same, thus our scaling law does not change. The driving force $F_{d,s} = -\mathrm{d}E/\mathrm{d}r = 2\pi\gamma(f-1)r$.

The resisting force is viscous shear force exerted on the substrate beneath the deposited film. Observing the side view of the liquid spreading through a forest of micropillars, we found that the pillar tops are hardly wet during the initial propagation of the wet front. The top surfaces get wet after the gaps between the pillars are filled with liquid, thus we only consider velocity profiles of the liquid between the pillars. Then the shear force exerted by the side of the pillars is scaled as $F_{r,1} \sim \mu U(f-1)(r^2-R^2)/d_s$, where $d_s = (s - \frac{\pi}{4}d)/2$ is a half the average distance between the adjacent pillars. The shear force by the base is scaled as $F_{r,2} \sim \mu U(1-f_t)(r^2-R^2)/h$. The total resisting force $F_{r,s} = F_{r,1} + F_{r,2}$ can be shown to have the form $F_{r,s} \sim \mu U(r^2-R^2)(f/h + c)$. We note that $c/(f/h)$ is typically smaller than 0.1 in our experimental conditions, thus we may write $F_{r,s} \sim \mu U(r^2-R^2)f/h$. In this estimation, we neglected the Oseen-type resisting force around a cylindrical pillar F_o, which scales as h. For $h < s$, $F_{r,s} \sim h^{-1}$ is known to dominate over $F_o \sim h$, which is consistent with our measurements.

As a liquid emits from a tube onto a hydrophilic surface, the viscous resistance occurs due to the interior wall of the tube as well as the substrate. The resisting force due to the tube wall is scaled as $F_{r,t} \sim 2\pi\mu R h_t U_t/R$, where U_t is the flow speed inside the tube and h_t is the liquid column height in the tube. U_t can be related to U via volume conservation: $\pi R^2 \mathrm{d}h_t = 2\pi r h(1-f)\mathrm{d}r$, so that $U_t = 2rh(1-f_t)U/R^2$. Because the resisting force due to the substrate is given by $F_{r,s} \sim \mu U r^2 f/h$ for $r^2 \gg R^2$, the ratio $F_{r,t}/F_{r,s} \sim 4h^2 h_t(1-f)/(R^2 r f)$, which is typically less than 0.05 for the substrates and the pens used in this work. Therefore, the friction at the tube wall can be neglected in evaluating the resisting force of the liquid flow.

The viscous resistance occurs due to the interior wall of the tube as well as the substrate, as a liquid emits from a tube onto a hydrophilic surface. The resisting force due to the tube wall is scaled as $F_{r,t} \sim 2\pi\mu R h_t U_t/R$, where U_t is the flow speed inside the tube and h_t is the liquid column height in the tube. U_t can be related to U via volume conservation: $\pi R^2 \mathrm{d}h_t = 2\pi r h(1-f)\mathrm{d}r$, so that $U_t = 2rh(1-f_t)U/R^2$. Because the resisting force due to the substrate is given by $F_{r,s} \sim \mu U r^2 f/h$ for $r^2 \gg R^2$, the ratio $F_{r,t}/F_{r,s} \sim 4h^2 h_t(1-f)/(R^2 r f)$, which is typically less than 0.05 for the substrates and the pens used in this work. Therefore, the friction at the tube wall can be neglected in evaluating the resisting force of the liquid flow.

Balancing this with the resisting force due to viscous shear stress which scales as $F_{r,s} \sim \mu U(r^2 - R^2)f/h$ gives $U = \mathrm{d}r/\mathrm{d}t \sim \phi\gamma r h/[\mu(r^2 - R^2)]$, where $\phi = (f-1)/f$. Integrating U yields $\hat{r}^2 - \ln\hat{r}^2 - 1 \sim \tau$, where $\hat{r} = r/R$ and $\tau = 2\phi\gamma h t/(\mu R^2)$. For narrow tubes and late times, corresponding to $r^2 \gg R^2$, this result simplifies to yield

$$r \sim \left(\phi\frac{\gamma}{\mu}h\right)^{1/2} t^{1/2}. \tag{2.1}$$

We see that an ink blot emerging from a pen spreads onto a stationary superhydrophilic surface with diffusive dynamics (Marmur, 1988), where in addition to the classically known prefactor (de Gennes *et al.*, 2004), $(\gamma h/\mu)^{1/2}$, the spreading rate depends on $\phi(f)$, the surface roughness. On real paper, the blot spreading is eventually limited by both contact line pinning at surface heterogenieties and evaporation. The spreading radii measured for different liquids and substrates collapse onto a single line with a slope of 0.51, consistent with our scaling law (2.1) (Fig. 2.2c).

We rearrange $U = \mathrm{d}r/\mathrm{d}t \sim \phi\gamma r h/[\mu(r^2 - R^2)]$ and integrate as the following:

$$\int_R^r \frac{r^2 - R^2}{r}\mathrm{d}r \sim \int_0^t \frac{\phi\gamma h}{\mu}\mathrm{d}t$$

For the purpose of comparison, we take the coefficient of proportionality to be unity and get

$$\left(\frac{r}{R}\right)^2 - \ln\left(\frac{r}{R}\right)^2 - 1 = \tau \tag{2.2}$$

where the dimensionless time $\tau = 2\phi\gamma ht/(\mu R^2)$. Figure 2.3 compares this result with the relationship approximating $(r^2 - R^2)/r \approx r$, i.e.

$$\frac{r}{R} = \tau^{1/2}$$

We see that the the error associated with approximating $(r^2 - R^2)/r \approx r$ in the integration vanishes as τ increases. For example, when $r/R = 10$, the relative error is less than 3%.

As a large area is wet due to wicking liquid, the evaporation may limit further spreading of the liquid in addition to the surface heterogenieties causing contact line pinning. Here we estimate the radius of a liquid blot, r_e, at which the evaporative loss of the liquid (over the entire blot area) becomes comparable to the liquid flux supplied by the tube. The evaporative mass flux of water vapor per unit area, $J(r)$, can be scaled as $J \sim D\Delta c/\delta$, where D and c, respectively, is the diffusivity and the concentration of vapor. $\delta(r)$ is the boundary layer thickness of the vapor concentration at the distance r from the center of the pen, scaled as $\delta \sim \sqrt{D(t-\tau)}$, where t and τ is the time taken for the liquid film to extend by r_e and r, respectively, from the moment of initial pen touch. Using $U(r) \sim \phi\gamma h/(\mu r)$ by virtue of Eq. (2.1), $t \sim \mu r_e^2/(\phi\gamma h)$ and $\tau \sim \mu r^2/(\phi\gamma h)$. Balancing the mass flux from the tube and the evaporative flux leads to

$$\rho U r_e h \sim \int J r \mathrm{d}r$$

where ρ is the density of the liquid. Then we get

$$r_e \sim \frac{\rho}{\Delta c}\left(\frac{\gamma\phi h^3}{\mu D}\right)^{1/2}$$

For the purpose of simple estimation, we adopt typical transport properties of water vapor $D \approx 2.6 \times 10^{-5}$ m^2/s and $\Delta c \approx 7 \times 10^{-3}$ kg/m^3 [F.P.

Incropera et al. *Fundamentals of Heat and Mass Transfer*, 6th ed. (2007)]. Then we get $r_e \sim 0.1 - 1$ m for water, which is much greater than typical size of the writing, providing justification for neglecting the effect of evaporation in the dynamics of liquid spreading considered here assuming that the evaporation properties of glycerine do not differ much from those of water. However, for real inks that are formulated to allow quick drying, D can be much greater than that of water thus it is possible that r_e is reduced to an order comparable to the ordinary ink writing.

Here we note that the spreading rate of an ink blot from a tube is different from that of a drop deposited on a hydrophilic surface. In drop spreading on micropatterned surfaces, a fringe film diffusively extends beneath the bulk part of the drop in a similar manner to (2.1), but the collapse of the bulk dominates the initial stages thus the entire drop footprint grows like $t^{1/4}$ (Kim *et al.*, 2011b). On smooth surfaces, a small drop spreads to become a thin lens with the radius growing like $t^{1/10}$ (Tanner, 1979). The ink blot from a tube spreads rapidly and diffusively on rough surfaces ($f > 1,\ \phi > 0$), while it does not spread on smooth surfaces ($f = 1,\ \phi = 0$). As shown in Fig. 2.4, a hydrophilic pen develops a capillary suction pressure $\Delta p_t = p_0 - p_t = 2\gamma/R - \rho g H$, where g is the gravitational acceleration and H is the liquid column height smaller than the equilibrium capillary rise height $2l_c^2/R$ with the capillary length $l_c = (\gamma/\rho g)^{1/2}$, which competes with the driving pressure $\Delta p_d = p_0 - p_e$ for spreading. Here p_0, p_t, p_e are the pressure beneath the tube, at the top of the liquid column in the tube, and at the outer edge of the blot, respectively. For a blot to spread beyond R on a rough surface, we should have $\Delta p_d|_{r=R} \approx F_{d,s}|_{r=R}/(2\pi R h) > \Delta p_t$, which gives a minimal roughness $f_{min} \approx 1 + 2h/R - Hh/l_c^2 \in (1.04 - 1.07)$ in our experimental conditions. On a smooth substrate, the maximum radius of a blot r_0 is given by $\Delta p_t = \Delta p_d$, where $\Delta p_d = \gamma(R_0^{-1} - r_0^{-1})$ with R_0 being the radius of curvature of a meniscus between the substrate and the tube

end that are separated by h_g. We numerically find that $r_0/R \in (1.05-1.5)$, which is indeed small, for $h_g/R \in (0-0.1)$ and $RH/l_c^2 \in (1-2)$.

2.4 Moving pen

2.4.1 Frontal shape

When writing, our interest is in predicting the frontal shape and the final width of the liquid film as a pen moves on the substrate with a constant velocity u_0, Fig. 2.5(a). We consider the coordinate system as shown in Fig. 2.5(b), where the liquid front moving with the pen intersects with a vertical line AB that is fixed to the substrate. The distance of the intersection P from the x-axis is denoted by w. We see that $\tilde{U} = \dot{w}\sin\theta$ corresponds to the radial velocity of the liquid front relative to the substrate. For a fan angled θ from the x-axis, the driving force of spreading in radial direction is given by $F_{d,m} = \gamma(f-1)r\Delta\theta$. The resisting force $F_{r,m}$ due to the radial velocity of a liquid film, $\tilde{U}$, is given by $F_{r,m} \sim \mu\tilde{U}(r^2 - R^2)\Delta\theta f/h$. Balancing $F_{d,m}$ and $F_{r,m}$ gives $\tilde{U} \sim \phi\gamma h/(\mu r)$. Because $\sin\theta = w/r$ and $\dot{w} = \dot{L}\mathrm{d}w/\mathrm{d}L$ with $\dot{L} = u_0$, we get the equation of the liquid front:

$$w \sim \eta(hL)^{1/2}, \tag{2.3}$$

where $\eta = (\phi/\mathrm{Ca})^{1/2}$ with the capillary number Ca defined as $\mathrm{Ca} = \mu u_0/\gamma$. Fig. 2.5(c) shows that the dimensionless liquid front profiles, w/R versus $\eta(hL)^{1/2}/R$, measured for different liquids and substrates indeed collapse onto a straight line with a slope 0.42. We emphasize that the parabolic front profile of (2.3) is different from that of the Rankine half body which is constructed by superposing a radially axisymmetric fluid source with a uniform flow. It is because the source strength is not axisymmetric in our case where the rate of liquid emission from the pen is governed by the front profile which is a function of θ. Also, the translation of the substrate with respect to the pen does not carry the entire liquid at the uniform velocity

but only drags the liquid touching the solid surface at u_0 while exerting shear stress over the liquid film of the thickness h.

The Rankine half body is constructed by the superposition of a point source and a uniform stream [G.K. Batchelor, *An Introduction to Fluid Dynamics* (1967) p. 461]. This process shows fundamental difference from ink writing. Uniform flow like effect in ink writing process is the bottom substrate movement under the this radial ink spreading. However, the substrate moving in specific speed only provides viscous shear force, but not the liquid moving in same speed, which gives obvious difference between the two.

When we superpose a diffusive point source producing a radial flow of magnitude $v_r = m/(2r)$, where m corresponds to the source strength, and a uniform flow u_0 in the horizontal direction, the stagnation streamline is given by $y = m(\pi - \theta)/(2\pi u_0)$. To see whether this matches the observed liquid front profile drawn by a moving pen, we take the two different source strengths. First, if we take the source strength of the stationary pen, $m \approx 0.13\phi\gamma h/\mu$ ($0.13 = 0.51^2/2$ is an empirical constant obtained via Fig. 2.2(c). Second, if we take the source strength to match the final line thickness w_f, $m = 2u_0 w_f$. Fig. 2.7(a) shows that the superposition of an axisymmetric source with a uniform stream predicts the line shapes (I and II) significantly different from the actually observed front profile. Even when we arbitrarily adjusted the location of the sources to match the stagnation point with the experiments, Fig. 2.7(b), the difference persists. The fundamental difference between the ink writing system and rankine half body lies on the process of computation.

2.4.2 Final width

Fig. 3.7 shows the (a) experimental image and (b) schematic side view of the edge of the liquid film laid out by a moving pen which is bounded by the outermost pillars of the wet area. The meniscus pinned at the pillars

of the boundary of wet area must overcome the energy barrier associated with contact line pinning in order to advance to the next row, which is unlikely due to the absence of liquid supply. Although the free energy of the system can be lowered to an extent by wetting another row, the pinning effect appears to dominate over this free energy reduction process as experimentally observed. The spreading of a liquid drop on hydrophilic micropillar array is investigated. And it is observed that the drop volume controls the size of the wetted area.

In a liquid trail where no more liquid is supplied as a pen moves away, the remaining film that has filled the gaps of the forest of micropillars stops advancing to the next row due to the contact line pinning at the boundary of the wet array as observed in experiment, so that the line width remains bounded. To obtain the scaling law of the line width w_f, we consider the volume of liquid that wets a shaded area in Fig. 2.8(a) in a given duration $\Delta\tau$. The volume, $\Delta\Omega = 2w_f u_0 h\Delta\tau$, is the sum of the amount of liquid that spreads outward on the surface, $\Delta\Omega_1$, and the volume of liquid that comes in direct contact with the substrate beneath the tube, $\Delta\Omega_2$, with $\Delta\Omega_1 \sim r\tilde{U}h\Delta\tau$, where $r\tilde{U} \sim \phi h\gamma/\mu$, and $\Delta\Omega_2 = 2Ru_0 h\Delta\tau$. Letting $\Delta\Omega = \Delta\Omega_1 + \Delta\Omega_2$, we find

$$\frac{w_f}{R} = \alpha\frac{\eta^2 h}{R} + \beta. \tag{2.4}$$

Fig. 2.8(b) shows that the experimentally measured line thickness scaled by R is indeed linearly proportional to $\eta^2 h/R$ with the slope (α) and the intersection with the y-axis (β) being 0.16 and 5.55, respectively.

Having quantified the dynamics of spreading of a simple liquid onto a periodically structured micropillar array, we turn to the mechanics of writing on paper, which is isotropic in plane but has strong variations in pore structure and tortuosity through the thickness. The square array used here is not perfectly isotropic but the anisotropy of flow on it was almost indiscernible as can be verified by the circular wet area of Fig. 2.2(a).

The fibers in paper guide two-dimensional liquid spreading, similar to that investigated here, thus simply modifying $\phi(\theta, z)$ will allow us to account for anisotropy and inhomogeneity of real paper. To make a quantitative comparison between our scaling law and the size of the ink blot and line on real paper as shown in Fig. 2.1, we estimate the liquid film thickness (or pore size) $h \approx 5$ μm and $\phi \approx 0.2$ based on the SEM image. The nib opening $2R = 0.1$ mm, and the ink has the surface tension $\gamma = 0.063$ N/m and viscosity $\mu \approx 3.8$ mPa·s (Drechsler *et al.*, 2010). When the pen is held for ~ 2 s, the radius of the blot is predicted to follow $r = 0.51(\phi\gamma ht/\mu)^{1/2} + 1.71R \approx 3.0$ mm and the line width with $u_0 \approx 5$ mm/s is to follow $r_f = 0.16\eta^2 h + 5.55R \approx 0.82$ mm, estimates which compare reasonably with the actual radius 1.3 mm and the width 0.7 mm. However, we note that the theory overestimates the blot radius more than it does for the line width, which is probably due to paper swelling.

2.5 Conclusions

In this chapter, we have constructed the scaling laws to describe the size and shape of an ink dot and line drawn by a pen on a superhydrophilic surface, and corroborated the results using experiments. Our experiments and scaling laws capture the basic hydrodynamics of ink writing associated with the spreading of a newtonian liquid on a porous substrate. Real inks are not newtonian and furthermore dry quickly; in addition modern pens are more sophisticated than the simple quill nibs of yore. In ballpoint pens, for example, the line width is set by the dimension of the ball and its mode of contact with paper, as a relatively viscous shear thinning ink that dries very quickly is spread out by a rolling ball. Understanding how to combine the dynamics of swelling and imbibition in soft porous media with the rate of deposition will allow us to extend the process of writing to the creation of functional porous surfaces on ever smaller scales.

Although our study focused on the spreading of ink supplied from a capillary tube, the end mechanisms of modern pens may complicate the physics. Also the study of ink spreading on three-dimensional fiber network, i.e. real paper, is naturally in order, where hemispherically driven capillary flows are resisted by viscous shear forces that follow Darcy's law. The scientific approach on the ink-spreading (or writing) process can help to develop better writing instruments and surfaces and to understand theoretically transport processes relevant to paper-based microfluidics.(Martinez *et al.*, 2008) Furthermore, the process of liquid front profile can be theoretically applied in other diffusion problems involving moving source.

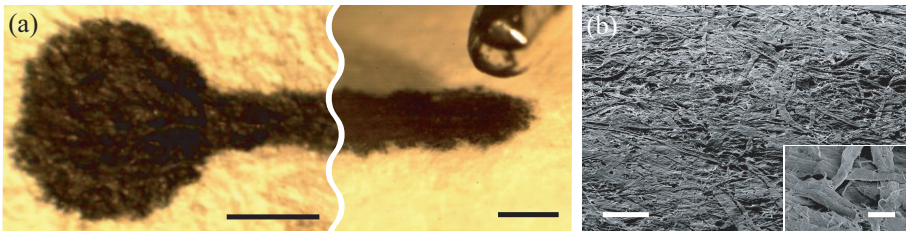

Figure 2.1: Images of ink trail and paper. (a) A blot (generated by holding the pen at a fixed position for about 2 s, top view) and the end of the line (tilted view) that is drawn with a modern fountain pen on rice paper. Scale bars, 1 mm. (b) Scanning electron microscopy (SEM) images of rice paper surface. Scale bar in the main panel and the inset, 150 μm and 10 μm, respectively.

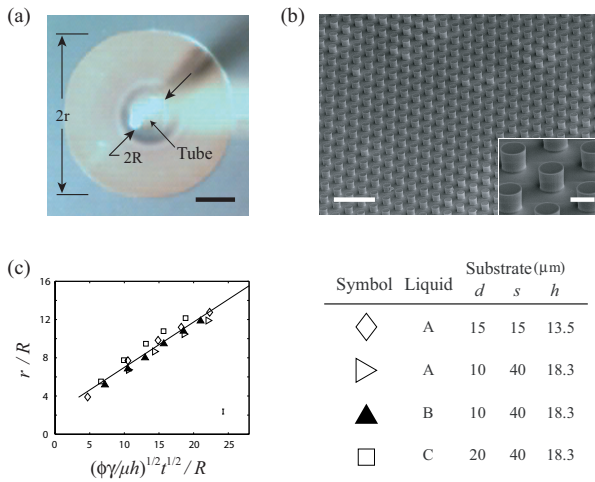

Figure 2.2: Blot formation on supherhydrophilic surfaces. (a) Top view of a liquid film emerging from a tube (which is out of focus) on a superhydrophilic surface. Scale bar, 1 mm. (b) SEM images of the superhydrophilic micropillar array. Scale bar in the main panel and the inset, 80 μm and 15 μm, respectively. (c) The scaled blot radius (r/R) plotted according to the scaling law (2.1). The slope of the best fitting straight line is 0.51, and the corresponding root mean square of deviation (RMSD) is 0.59. A characteristic error bar is shown in the lower right corner.

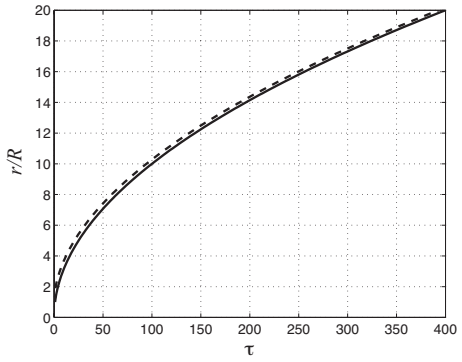

Figure 2.3: Comparison of the radial evolution models of a blot with (broken line) and without (solid line) including the tube radius R.

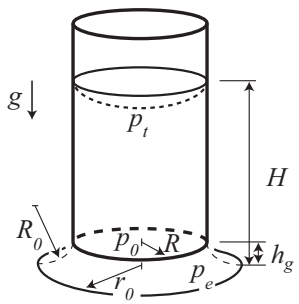

Figure 2.4: Schematic of a small blot emitting from a tube on a smooth surface which is limited by the competition of the capillary suction pressure inside the tube and the Laplace pressure at the outer rim of the blot.

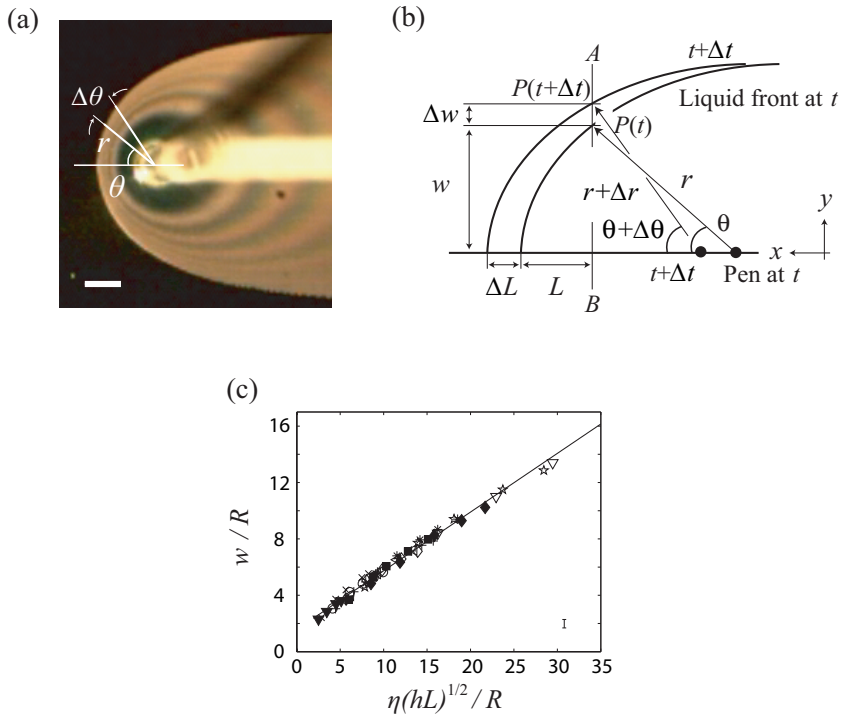

Figure 2.5: Lines drawn by a moving pen. (a) A snapshot of the liquid film spreading on a substrate as emitting from a moving pen. Scale bar, 1 mm. (b) The coordinate system to describe the shape of the liquid front. (c) The scaled film profile (w/L) plotted according to the scaling law (2.3). The slope of the best fitting straight line is 0.42 with RMSD=0.16. The experimental conditions for each symbol are listed in Fig. 2.6. A characteristic error bar is shown.

Symbol	Liquid	u_0 (mm/s)	R (mm)	Substrate (μm) d	s	h	f
◁	A	2.5	0.5	15	30	13.5	1.71
■	B	0.8	0.5	15	30	13.5	1.71
◆	B	0.3	0.5	10	40	18.3	1.36
×	C	1.3	0.5	15	30	13.5	1.71
○	C	0.8	0.5	10	40	18.3	1.36
◇	C	0.8	0.5	20	40	18.3	1.72
▼	C	0.8	0.5	10	40	9.0	1.18
▽	D	0.8	0.25	15	30	13.5	1.71
✳	D	0.8	0.4	15	30	13.5	1.71
☆	D	0.8	0.75	15	30	13.5	1.71
+	D	0.8	0.1	15	30	13.5	1.71

Figure 2.6: Experimental conditions for the symbols in Figs. 2.5(c) and 2.8(b).

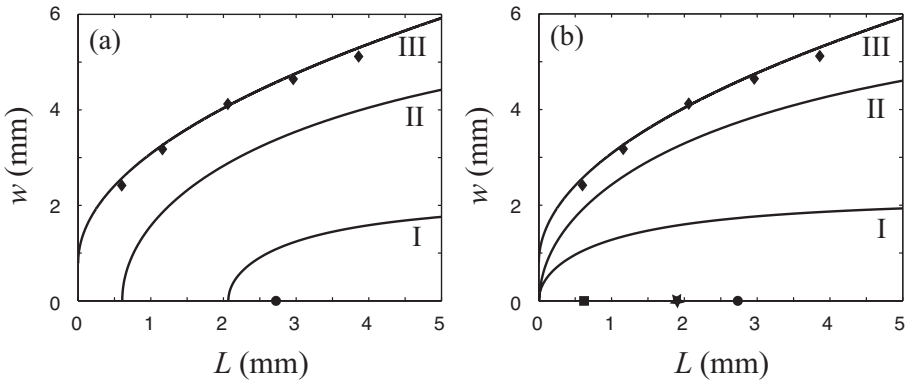

Figure 2.7: Comparison of the Rankine-half bodies and the actual front profile of the line (liquid B) drawn by a pen of $R = 0.5$ mm moving with $u_0 = 0.3$ mm on the substrate with $[h, d, s] = [18.3, 10, 40]$ μm. Lines I and II are the predictions of the Rankine half body model which match the source strength of the stationary pen and the final line width, respectively. Line III is the parabolic profile of this work with the empirical parameters obtained via Fig. 2.5(c). Diamonds are the experimental measurements. (a) The locations of the actual pen and the sources of the Rankine half body model coincide. (b) The source locations (a square for line I and a star for line II) have been adjusted to match the stagnation point at the origin. The filled circles in (a) and (b) correspond to the location of the pen.

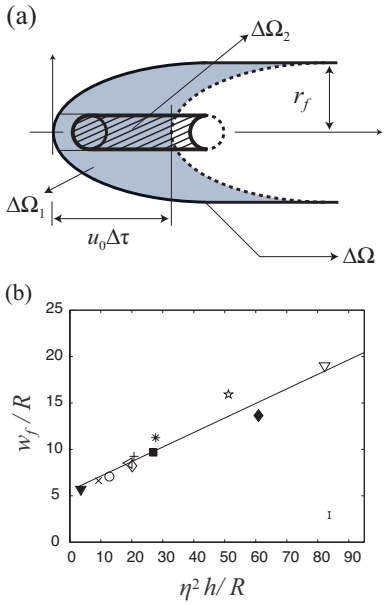

Figure 2.8: (a) The shaded area wet by ink for a duration $\Delta\tau$, equals to $2r_f u_0 \Delta\tau$. (b) The dimensionless line thickness w_f/R scales linearly with $\eta^2 h/R$ regardless of liquid, pen speed, tube radius, and pillar array dimensions. The slope of the best fitting straight line is 0.16 and its extension meets the y-axis at 5.55 with RMSD=0.95. The experimental conditions for each symbol are listed in Fig. 2.6. A characteristic error bar is shown.

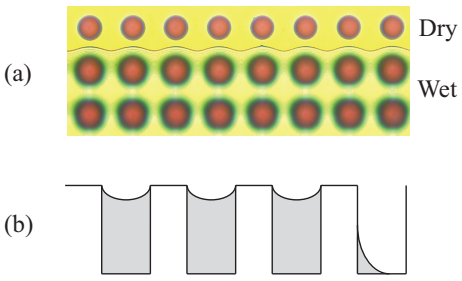

Figure 2.9: (a) Top view of the edge of the film of liquid C on the micropillar array with $[h, d, s] = [13.5, 15, 30]$ μm. (b) Schematic of the side view of the edge of the liquid film.

Chapter 3

Dynamics of hemiwicking

3.1 Introduction

Recent development in micro- and nanoscale surface patterning technology has made it possible to obtain tailored topography of solid surfaces as well as wide range of wettability. This allows us to investigate novel liquid-solid interaction behavior, which is qualitatively different from the dynamics of liquids on smooth solid surfaces. On microtextured hydrophobic surfaces, drops roll (Mahadevan & Pomeau, 1999; **?**) rather than slide. Drops bounce (Bird *et al.*, 2013; Richard & Quéré, 1999) or fragmentize (Tsai *et al.*, 2009) upon collision with the super-water-repellent surfaces depending on impact conditions. When a drop is deposited on microdecorated hydrophilic surfaces, the liquid wicks into the gaps of protrusions, a behavior termed hemiwicking (Bico *et al.*, 2002). Hemiwicking on the superhydrophilic surfaces leads to a variety of intriguing flow characteristics, such as polygonal spreading (Courbin *et al.*, 2007), zippering wetting front (Kim *et al.*, 2011b), and enormously promoted rise of liquid film against gravity (Xiao *et al.*, 2010).

Here we consider the rate of liquid film climbing a rough hydrophilic substrate that touches a liquid bath. Since the flow speed and film thickness are so small that the inertia and gravity can be neglected compared to

the viscous resistance, the rate of hemiwicking is determined by the balance between the driving capillary forces and the resisting viscous forces. Thus, the fundamental physics does not differ from a capillarity-driven tube imbibition problem (Washburn, 1921), and a simple scaling law can be readily constructed as Ishino et al. (2007) explained as the following (Ishino *et al.*, 2007). As the capillary force is scaled as γa, where γ is the liquid-gas surface tension and a is the lengthscale that generates the capillary effect, and the viscous force is scaled as $\mu L\dot{L}$, where μ is the liquid viscosity, L is the imbibition distance from the source, and overdot is the time derivative, the force balance leads to a diffusive rule for L: $L \sim (Dt)^{1/2}$, where the effective diffusivity $D \sim \gamma a/\mu$. A number of studies on the hemiwicking on superhydrophilic substrates found that the imbibition length indeed grows like $(Dt)^{1/2}$.

However, rough substrates cannot be described by a single geometric parameter like a tube with a constant radius a. For example, a square array of circular micropillars should be described by the following three parameters: height, diameter, and spacing of the pillars. As a result, different forms of effective diffusivity were suggested by different authors for regular micropillar arrays, which were shown to be valid for the specific experimental conditions employed in each work. Below we find that those suggested diffusivities hold in limited conditions only, implying that the most general understanding on the hydrodynamics of hemiwicking has not been achieved yet. Goals of the current study are three-folded. First, we aim to construct a universally valid scaling law for hemiwicking and experimentally corroborate the model. Second, we discuss the effects of pillar arrangements, or the *skewness* of pillar lattice, on the hemiwicking flows. Finally, we find the maximum pillar spacing up to which the current assumption of densely spaced pillars is valid.

	Liquid	γ (N/m)	μ (Pa·s)
A	Water	0.073	0.0013
B	Silicone oil	0.020	1.050
C	Ethylene Glycol 99 wt%	0.048	0.018

Table 3.1: Liquid properties at about 23°C.

3.2 Experiments

To fabricate rough hydrophilic substrates, we etch an Si wafer using the deep reactive ion etching process, which results in pillar arrays of various geometric parameters depending on designs of photomasks and etching durations. The pillar arrays are coated with the Si-incorporated diamond-like carbon film using the gas mixture of benzene and silane in a radio frequency chemical vapour deposition chamber. Then the surfaces are plasma-etched by oxygen to turn superhydrophilic owing to hydrophilic Si-O bonds and nanoscale roughness. For more detailed process conditions, see Yi *et al.* (2010) (Yi *et al.*, 2010). As shown in Fig. 3.1(a), the individual pillars are cylindrical with height h and diameter d, and arranged with transverse and longitudinal pitches s_1 and s_2, respectively.($s_1 > d$ and $s_2 > d$) The *skewness* of array is determined by α which can vary from 0 to $\tan^{-1}(s_1/s_2)$. In our experiments, h and d range from 2.9 to 20 μm, s_1 and s_2 from 15 to 225 μm, and α from 0 to 60°. As reservoir liquids, we use water, silicone oil(1000 cst), and Ethylene Glycol 99 wt%, which are listed in table.5.1 All the liquids completely wet the micropillar arrays, so that the equilibrium contact angle of the liquids with the surfaces is nearly zero. As the substrate, whose area measures approximately 4×50 mm^2, touches the reservoir liquid, the liquid film climbs the surface, which is recorded by a CCD (charge coupled device) camera at a frame rate up to 500 s^{-1}.

While the front edge of the rising liquid film appears fairly straight when viewed from a distance as in Fig. 3.3(a), close observations reveal

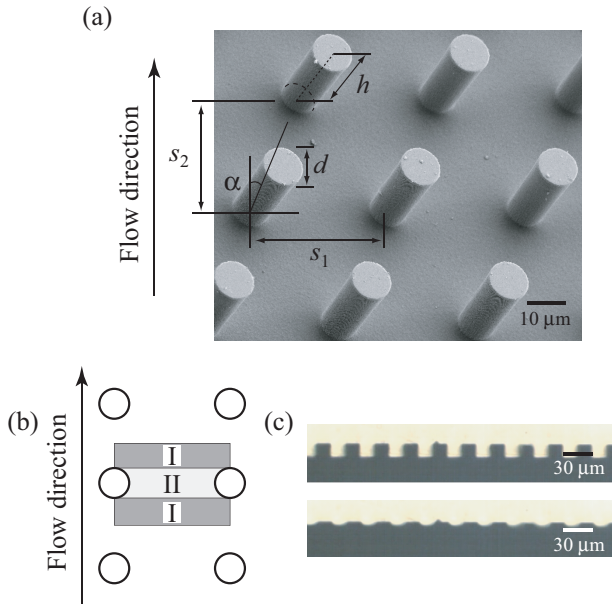

Figure 3.1: (a) Geometric parameters of a cylindrical pillar array. (b) SEM (scanning electron microscopy) image of a microwall array of Si. (c) Side view of the microarray before (upper image) and after (lower image) being impregnated by a liquid.

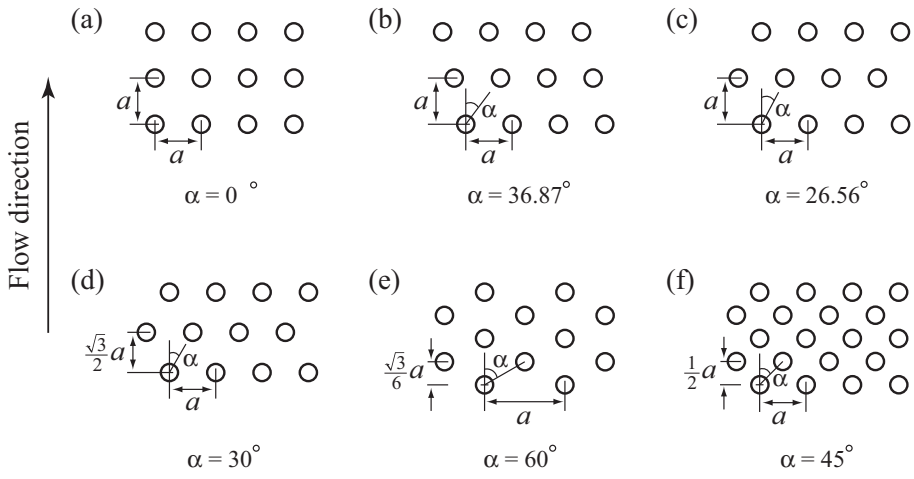

Figure 3.2: Schematic diagram of micropillar arrays. Even the same structures can bring different results as flow directions.

complicated advancing dynamics originated from the presence of pillars. On rectangular arrays with $\alpha = 0$, the lateral propagation of a protruding step, or zipping, must occur before the contact line advances to the next row of pillars (Courbin *et al.*, 2007; Kim *et al.*, 2011a) as shown in Fig. 3.3(b). On skewed arrays as displayed in Fig. 3.3(c), liquid film apparently radiated from each pillar drives the advance of contact line against gravity. In the following, we construct a scaling law to predict the advancing speed of the seemingly straight interface edge, and then investigate the microscopic dynamics of liquid meniscus determined by the pillar arrangement.

3.3 Macroscopic model of hemiwicking dynamics

We consider the advancing rate of a liquid film on a superhydrophilic textured substrate that touches a reservoir liquid. The film thickness is defined by the pillar height, and the Reynolds number is given by $Re = \rho U h/\mu$, where U is the rise speed. Re is typically $O(10^{-10} - 10^{-2})$ in our

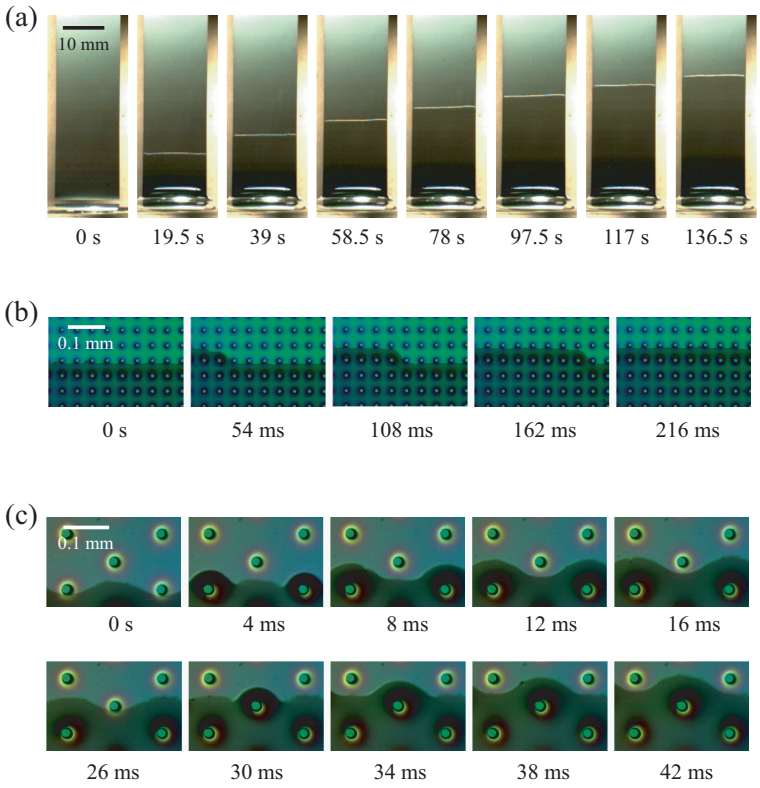

Figure 3.3: (a) Macroscopic view of liquid rise due to wicking within an array of micropillars. (b) Magnified view of liquid rise on a rectangular pillar array with $\alpha = 0$ and $\{h, d, s_1, s_2\} = \{7.2, 10, 40, 40\}$ μm. (c) Magnified view of liquid rise on a skewed pillar array with $\alpha = 60°$ and $\{h, d, s_1, s_2\} = \{20, 20, 216.5, 62.5\}$ μm

experiments, allowing us to ignore the effects of inertia as compared to viscosity. The Bond number, defined by $Bo = \rho h^2 g/\sigma$, with g being the gravitational acceleration, is $O(10^{-7} - 10^{-4})$, implying negligible effects of gravity. The flow is driven by capillary forces at the rising front. The change in the surface energy associated with the advance of the liquid front by $\mathrm{d}L$ is given by: $\mathrm{d}E = \{\gamma[1 - \frac{\pi}{4}d^2/(s_1 s_2)] + (\gamma_{SL} - \gamma_{SG})[f - \frac{\pi}{4}d^2/(s_1 s_2)]\}\mathrm{d}L$, where f is the roughness defined as the ratio of the actual solid surface area to the projected area, γ_{SL} is the interfacial tension between solid and liquid, and γ_{SG} is that between solid and gas. Upon the basis of Young's equation, $\gamma\cos\theta = \gamma_{SG} - \gamma_{SL}$, we get $\mathrm{d}E = -\gamma(f-1)\mathrm{d}L$. The driving force can be estimated as $F_d = -\mathrm{d}E/\mathrm{d}L$ assuming that the pillar diameter and pitches are negligibly small compared to the rise height, so that we get $F_d = (f-1)\gamma$.

Negligibly small effects of inertia imply that the driving force is balanced by the resisting viscous force. Observing the side view of the liquid spreading through a forest of micropillars, Fig. 3.1(c), we find that the tops of the pillars are hardly wetted as the wet front propagates. Although we do not preclude the possibilities that the top surfaces become wet slowly as the liquid meniscus climbs the pillars over a long time, it would hardly affect the rate of wetting that occurs at the propagation front. To evaluate the shear force exerted by the substrate base, $F_{r,1}$, we simply assume the average flow speed of U in region I and U' in region II of Fig. 3.1(b). Continuity allows us to write $U' = 2Us_1/d_s$, where the average distance between the adjacent pillars $d_s = s_1 - \frac{\pi}{4}d$. Then $F_{r,1} \approx \mu[Us_1(s_2 - d)/h + U'dd_s/(2h)](L/(s_1 s_2)) \sim \mu UL/h$, where $\sim$ signifies "is scaled as" and L is the rise height of the liquid film. The shear force exerted by the pillar side, $F_{r,2} \approx 2\mu U'dhL/(s_1^2 s_2) \sim \mu UL(h(f-1)/s + c)/h$ with $s = s_1 - d$. We note that $c/[1 + h(f-1)/s]$ is typically smaller than 0.1, thus we may write the total resisting force as $F_r = F_{r,1} + F_{r,2} \sim \mu UL[1 + h(f-1)/s]/h$. Additional resisting forces arise in the vicinity of

the contact line where the shear force tends to infinity if a classical no-slip boundary is applied (Huh & Scriven). Using a cutoff length $\lambda \sim 1$ nm to avoid the contact line singularity, the shear force near the contact line is scaled as $F_c \sim \mu U \ln(s/\lambda)/\theta$, where the advancing contact angle $\theta \approx 5°$. As $F_c/F_r < O(0.1)$ for $L > 5$ mm, we neglect the effects of the wedge dissipation near the contact line.

Balancing F_d and F_r gives the speed of the hemiwicking front U as $U = \mathrm{d}L/\mathrm{d}t \sim \eta\gamma h/(\mu L)$, where the dimensionless coefficient η is specified solely by the pillar structure: $\eta = (f-1)/[1+h(f-1)/s]$. Integrating the preceding relation for L yields

$$L \sim \left(\eta \frac{\gamma}{\mu} h\right)^{1/2} t^{1/2}. \tag{3.1}$$

While a similar scaling relation that reveals the diffusive dynamics of a hemiwicking front on micropillar arrays was reported earlier (Kim *et al.*, 2011a,b), here we suggest a generalized coefficient η, which is not restricted to a case where $h \approx s$ as in the previous works. We compare this theoretical prediction with the experimental results obtained with various pillar arrays and different liquids in the following.

Fig. 3.4(a) shows that the propagation distance of wetting front increases linearly with $\sqrt{t}$ for various pillar arrays and liquids, but with different slopes. In particular, the diffusive dynamics is observed to hold even for skewed lattices. The schematic diagrams of the lattice configuration are demonstrated in Fig. 3.2. We see in Fig. 3.4(b) that the current scaling law (3.1) makes all the data collapse onto a single straight line. In the plot, we scaled the distance L with the capillary length $l_c = [\gamma/(\rho g)]^{1/2}$, which corresponds to the characteristic height of the meniscus touching a smooth hydrophilic vertical wall. Our scaling law is seen to be valid regardless of skewness of the pillar lattices despite obvious differences in microscopic flow characteristics as demonstrated in Fig. 3.3. Fundamentally, the flows of this study are classified as an inertia free flow. Mathematically, there is no

term of flow speed gradient in flow direction, meaning that the dynamics is only determined by the instant state itself, not by the previous movement. Accordingly, the total number of pillars with uniform longitudinal distance is important for both of the driving force and resiting force, while the relative location of the pillars from the previous row is not a dominant factor. (See inset of Fig. 3.4(b)) Thus, the skewness which determines the location does not seriously affect the flow dynamics.

Our scaling law with the structure coefficient is compatible with other theories, by considering ranges of aspect ratio of the gap (s) and pillar height(h). When the gap is much larger than pillar height, η is approximately equal to $f-1$. Then, our theory is identical to another theory of Quéré for the same condition (Ishino *et al.*, 2007). If the pillar as high as the gap, $\eta \approx 1-1/f$ (Kim *et al.*, 2011a). As the pillar height is much larger than the gap, dominant resisting force takes place on pillar walls, which leads the $\eta \sim s/h$. According to the Quéré's theory, the imbibition coefficient is similar to $D_{qu} \sim (\gamma/\mu)d(\ln(d/s+1)-1.31)$, and the coefficient based on our theory is $D_{th} \sim (\gamma/\mu)s$. For wide range of ratio of d and s, $(4 < s/d < 100)$, $D_{th}/D_{qu} \sim O(1)$, where the equal condition $(D_{th} = D_{qu})$ is established when $\ln(d/s+1)-1.31 \approx \pi s/d$.

3.4 Microscopic model of hemiwicking dynamics

A major assumption underpinning the foregoing scaling law, (3.1), is that the wetting flow is continuously driven by surface roughness. Due to the continuity of the assumption, given an infinitesimal length scale $\epsilon \ll L$, speeds of $L+\epsilon$ and $L-\epsilon$ are identically estimated as $\sim \eta\gamma h/(\mu L)$, by the scaling law (3.1). However, by the microscopical experiments of wide longitudinal gap, s_2-d, the interfacial speeds passing a pillar instantly and sweeping the substrate base sufficiently far from the pillar are obviously different, as shown in Fig. 3.3(b) and (c). For solving the inequality of the macroscopic law and the microscopic experimental result, we aim to analyze

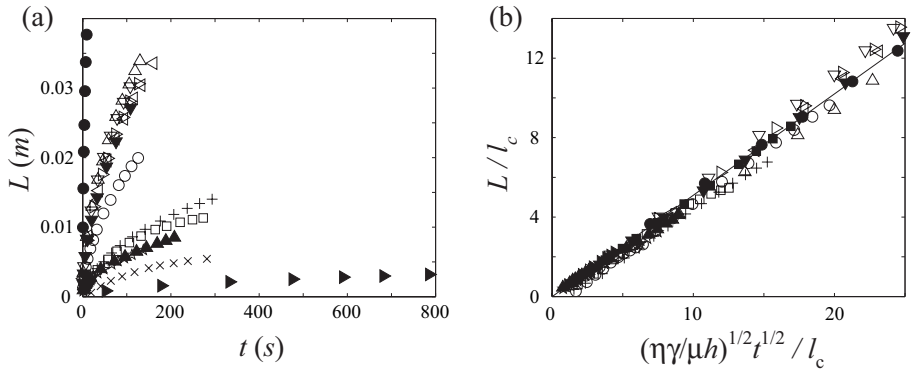

(c)

Symbol	Liquid	Substrate (μm) Array	s_1	s_2	d	h	α (°)	f
●	A	(*a*)	40	40	20	26	90.0	2.02
▶	B	(*a*)	40	40	20	9	0.0	1.35
▼	C	(*a*)	40	40	10	26	0.0	1.51
▲	C	(*a*)	20	20	10	2.9	0.0	1.23
■	C	(*a*)	15	15	10	26	0.0	4.63
◁	C	(*b*)	40	40	10	26	36.9	1.51
▷	C	(*c*)	40	40	10	26	25.6	1.51
▽	C	(*d*)	40	34.6	10	26	30.0	1.59
☆	C	(*e*)	43.3	12.5	10	3.4	60.0	1.20
○	C	(*e*)	43.3	12.5	10	10	60.0	1.58
+	C	(*e*)	129.9	37.5	20	10	60.0	1.12
×	C	(*e*)	303.1	87.5	20	10	60.0	1.02
□	C	(*e*)	216.5	62.5	10	20	60.0	1.05
△	C	(*f*)	40	20	10	10	45.0	1.39

Figure 3.4: (a) Propagation distance of the liquid-air interface versus $\sqrt{t}$. (b) The scale wetting distance (L/l_c) plotted according to the scaling law (3.1). The slope of the best fitting straight line is 0.49. (c)Experimental conditions for the symbols

the microscopical propagation to approach the scaling law (3.1) in different manner and examine the assumptions implicitly used in the macroscopic scaling model. Additionally, using the comparison analysis of macro and micro scaled models, we aim estimate the validation limit of the scaling law (3.1), as well, in this section.

For the microscopic point of view, we start from employing the lubrication theory since the flow forms thin wide film. Here, the theory is slightly modified, by using an adjustment parameter, $(f-1)/\eta$, because the flow is resisted by pillar side as well as substrate base. The adjustment parameter, ratio between the shear stress of actual surface and the shear stress of ideally smooth substrate with film thickness being h, is already derived in macroscopic model. So and denoting the local flow speed, $U_{lo}(x)$ for local propagation distance x, (See Fig. 3.5(a)) the modified lubrication relation is written as

$$\frac{\mathrm{d}p(x)}{\mathrm{d}x} \sim \mu \frac{f-1}{\eta} \frac{U_{lo}(x)}{h^2}. \tag{3.2}$$

Using the linear assumption of the pressure gradient, $\mathrm{d}p(x)/\mathrm{d}x \sim (p(0) - p(x))/x \sim (p_0 - p(x))/(L+x)$ and mean force relation $h(p_0 - p(x)) \sim -\mathrm{d}E(x)/\mathrm{d}x$ (Srivastava *et al.*, 2010), the pressure gradient term is scaled as

$$\frac{\mathrm{d}p(x)}{\mathrm{d}x} \sim -\frac{\mathrm{d}E(x)}{\mathrm{d}x} \frac{1}{Lh}, \tag{3.3}$$

since $L \gg x$. These approximations are reasonable because the film thickness is uniform and approximately equal to the pillar height, as shown in the side view images of Fig. 3.1(c).

In case of the macroscopic model, varying local driving force is not addressed but mean driving force is employed, which gives

$$F_d = (1/s_2) \int_0^{s_2} \frac{\mathrm{d}E(x)}{\mathrm{d}x} \mathrm{d}x = \frac{E(s_2) - E(0)}{s_2} = \gamma(f-1). \tag{3.4}$$

Furthermore, varying local speed cased by the varying local driving force is not addressed, either, but mean flow speed is employed as

$$U = (1/s_2)\int_0^{s_2} U_{lo}(x)\mathrm{d}x. \tag{3.5}$$

Considering the scaled pressure gradient term (3.3) and integrating the modified lubrication relation yields,

$$\int_0^{s_2} -\frac{\mathrm{d}E(x)}{\mathrm{d}x}\frac{1}{Lh}\mathrm{d}x \sim \int_0^{s_2} \mu\frac{f-1}{\eta}\frac{U_{lo}(x)}{h^2}\mathrm{d}x. \tag{3.6}$$

Substituting the corresponding terms for the mean driving force and mean speed, the scaling law of flow speed in the macroscopic model is derived as $U \sim (\gamma h)/(\mu L)$, which is identical to the macroscopic model. For the microscopic analysis, the mean value relations (3.4) and (3.5) are not used but varying driving force and speed are addressed. Thus, the microscopic movement for the interface is mainly focused.

When liquid interface reaches the bottom of a pillar, the liquid starts to wet the pillar since wet state is energetically more stable than dry state. At the beginning of the wetting, the liquid climbs up the pillar and spreads on the substrate simultaneously, as shown in Fig. 3.5(b), which is referred to as *climbing*. When the liquid perfectly wets the pillar, *climbing* stops but the spreading keeps preceding by the next pillar, which is referred to as *sweeping*, as shown in Fig. 3.5(b). The starting point of *sweeping* is indicated as $x = x_0$ in Fig. 3.5(b). While *climbing*, capillary force arises at the interface by wetting pillar side, which drives the liquid flow. The driving force per unit width derived by the energy change rate is $-\mathrm{d}E/\mathrm{d}x = -\mathrm{d}E/\mathrm{d}y(\mathrm{d}y/\mathrm{d}x) = F_c(\mathrm{d}y/\mathrm{d}x)$ by the chain rule, where F_c means climbing force. Considering $F_c \approx \pi d\gamma/s_1$ and $\mathrm{d}y/\mathrm{d}x \sim h/s_2$, the driving force is scaled as $\sim \gamma\pi d/(s_1 s_2) = \gamma(f-1)$. Combining this relation with the form (3.3), the pressure gradient term of the modified lubrication relation (3.2) is written as $\gamma(f-1)/(Lh)$; thus, the local propagation speed of the *climbing* is as follows,

$$U_{lo}(x) \sim \eta \frac{\gamma h}{\mu L}, 0 < x \leq x_0. \tag{3.7}$$

As shown in the scaling law above, the speed of microscopic model of *climbing* is identical to that of the microscopic model. (See the section 3) However, when the liquid trace rises up the pillar completely, *sweeping* starts and the frontal speed slows down, since pillar effect on driving force becomes smaller than that of the *climbing*. The liquid front end keeps spreading the substrate base fixing the other end at the pillar top edge. The pressure drop is roughly evaluated by geometrical model of front meniscus in Fig. 3.5(b). The radius of curvature of the meniscus is roughly $R(x) \approx (h^2 + x^2)/(2h)$ and is inversely proportional to the instant pressure drop, $\gamma/R(x)$. Considering that the pressure drop take places at the vicinity of the pillar, the mean pressure gradient for unit width is scaled as $\sim \gamma/(LR(x))(d/s_1) \approx h\gamma/(L(x^2+h^2))(d/s_1)$. Substituting this form for the pressure gradient term in the modified lubrication relation (3.2), the scaling law of *sweeping* speed yields,

$$U_{lo}(x) \sim \eta \frac{\gamma h}{\mu L} \frac{s_2 h}{x^2 + h^2}, x_0 < x. \tag{3.8}$$

In contrast to the *climbing*, the scaling law (3.8) shows obvious difference from the macroscopic model. The relations (**??**) and (**??**) give two asymptotic lines, $x \sim \{(\gamma/\mu)\eta h/L\}t$ for $0 < x \leq x_0$ and $x \sim \{(\gamma/\mu)\eta d h^3/s_1/(f-1)/L\}^{1/3} t^{1/3}$ for $x_0 \ll x$, respectively, which show good agreement with experimental data points in Fig. 3.5(c)and (d) for a rectangular array and a hexagonal array, respectively. Insets of Fig. 3.5 (c) and (d) show the power laws of the two regimes.

To predict the validation limit of the scaling law (3.1) quantitatively, it is necessary to investigate microscopic behavior of liquid spreading. When liquid reaches pillar bottom, liquid starts to spread radially. Due to the isotropy, the liquid trace moves toward any of dry pillars at the front and

the pillar that the liquid touches becomes next foothold for the successive spreading. If only *climbing* takes place before it reaches the next pillar, the speeds of the macroscopic model (3.1) and microscopic model (3.7) are identical, implying that our scaling law (3.1) is valid. However, if both of *climbing* and *sweeping* occur, as *sweeping* starts, the local speed of microscopic model (3.8) begins to deviate from that of the macroscopic model implying that the scaling law (3.1) is invalid. Thus, comparison of x_0 and the distance for reaching the next pillar, the minimum distance (p_{min}), is important to determine the validity. The minimum distance is $p_{min} = min(s_2/\cos\alpha, \sqrt{(s_2/\cos\alpha - s_1\sin\alpha)^2 - s_1^2\cos^2\alpha})$ given by geometrical analysis. Letting $w = p_{min} - d$ and using dimensionless components $\zeta = h/w$ and $\lambda = d/w$, topographic assumption, $x_0 \sim h$, gives the propagation distance ratio, $\Pi = x_0/p_{min}$ as

$$\Pi \sim \frac{\zeta}{1+\lambda} \tag{3.9}$$

Fig. 3.6 shows a map describing the experiments using dimensionless parameters w/d and h/w with the boundary line of (3.9) and the experimental data points. As shown in this figure, the valid data points and the invalid data points are well separated by the boundary theory. Given the pillar properties h and d, sparser pillar array (larger w) results in a longer *sweeping* distance, whereas denser array (smaller w) reduces the distance. Pillar diameter also slightly affects the validity. If the diameter is remarkably large, it also enlarges the *sweeping* distance.

3.5 Conclusions

In this chapter, we have experimentally and theoretically studied capillary rise of a liquid deposited on a single substrate with micro pillar arrays. We prepared dozens of different substrates with cylindrical pillar arrays and observed the macroscopic and microscopic behavior of the capillary rise of

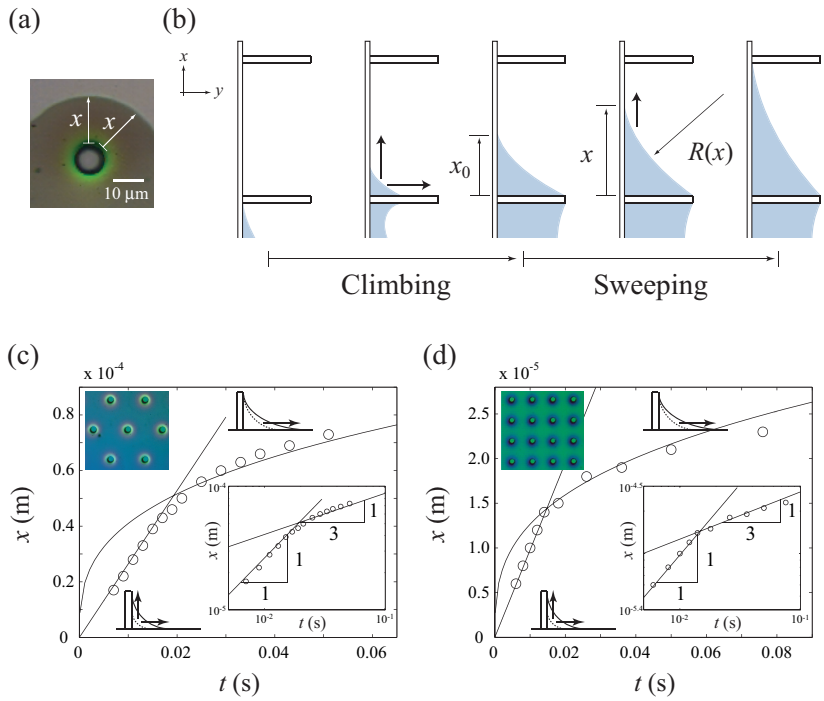

Figure 3.5: (a) Simplified model of liquid sweeping process between pillars. (b) Schematic diagrams of microscopic advancing process, which include climbing a pillar and sweeping on the bottom. (c) and (d) Plots of advancing distance between pillars with (c) $L = 5$mm, $\alpha = 60°$, and $\{h, d, s_1, s_2\} = \{20, 20, 216.5, 62.5\}$ μm and (d) $L = 20$mm, $\alpha = 0°$, and $\{h, d, s_1, s_2\} = \{7.2, 10, 40, 40\}$ μm. Insets show logarithmic plots of the two cases where the arithmetic average of the slopes of the best-fitted lines are 0.997 and 0.368 for (c) and 1.000 and 0.308 for (d), respectively.

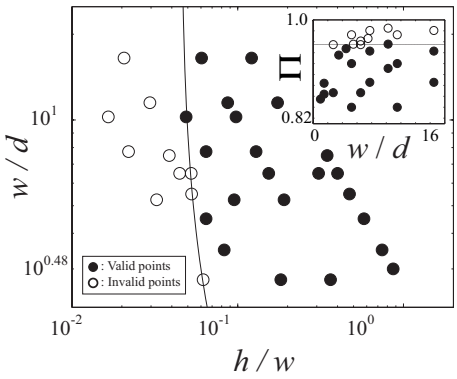

Figure 3.6: Scope of experiments of this study with the propagation distance ratio curve, $\Pi \approx 0.07$ (Inset) Separation of experimental data by the ratio. Circle and triangle marks indicate valid and invalid points of scaling law (3.9), respectively.

a few liquids. The macroscopical liquid movement seems to be smoothly deposited, but it involves intrigue microscopical liquid spreading according to the pillar arrays. Scaling analysis has been performed for the dynamics of interfacial propagation distance by using surface tension force and resisting shear force and it is shown that the macroscopic propagation follows Washburn's law ($L \propto t^{1/2}$). Inertial force is neglected due to small film thickness (micro-scale) and low flow speed and the gravitational force is also neglected in the range of our interfacial height interest (smaller than 5cm) of this scaling analysis. In this study, we focused on the structural dependency as a function of the unit pillar height, diameter, and pitch, as well as the pillar configuration, which is quantified by the structure coefficient $\eta = (f-1)/[1+h(f-1)/s_1]$ in our scaling law (3.1). Skewness of the pillar rows has been also investigated, but cases with different skewness do not show any significant difference for same longitudinal and transverse pitches (s_1 and s_2). Also, separating the microscopic propagation by *climbing* and *sweeping*, we derive scaling laws of the spreading dynamics, which are verified by experiments. Comparing results of the macroscopic model

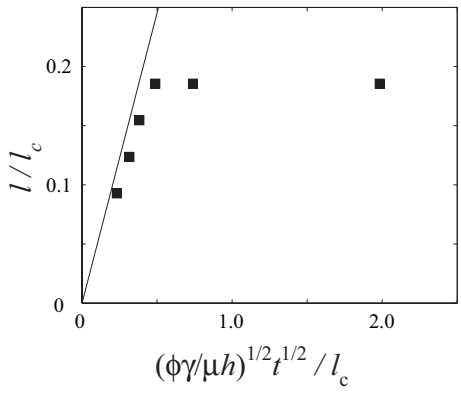

Figure 3.7: Rise height is limited by gravity. The pillar configuration of the substrate is rectangular where s_1, s_2, d, h and f are 75 μm, 75 μm, 10 μm, 2.9 μm and 1.016, respectively. The line slope is 0.49, which is the same straight line in the figure 3.4

and microscopic model, we derive a scaling law of the validation limit of the scaling law (3.1) deduced through the macroscopic model.

In experiments, we observed that the gravity is negligible at the beginning, whereas it is no longer negligible when the liquid reaches high. At this moment, the propagation stops, as shown in Fig. 3.7. The height limit is simply derived by considering the meniscus propagation between pillars. The negative pressure that the meniscus generates gets smaller until it reaches the next pillar and the minimum pressure drop is estimated as $\sim \gamma h/(h^2 + w^2)$. When it cannot overcome the hydrostatic pressure, the propagation stops and the critical height (H_{cri}) is predicted by balancing the two pressures, which is $H_{cri} \sim \gamma h/(\rho g(h^2 + w^2))$.

Although the flow along the rectangular pillar arrays regularly has been studied intensively, the flow in different direction such as diagonal directional flow has not been investigated yet, but proposed theories using roughness term with pillar dimensions that are independent of the direction. However, the longitudinal pillar gap s, perpendicular to the flow direction,

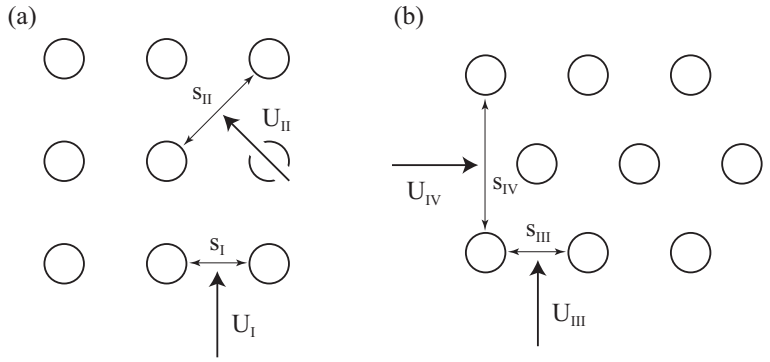

Figure 3.8: Schematic diagrams of different directional flows when the substrates are (a) rectangular (U_I and U_{II}) and (b) hexagonal pillar arrays (U_{III} and U_{IV}). $s_I < s_{II}$ and $s_{III} < s_{IV}$ result $U_I < U_{II}$ and $U_{III} < U_{IV}$, respectively because larger gap causes resisting force smaller in spite of same roughness and pillar dimensions.

is a critical factor to determine the flow resistance, inversely proportional to the distance between pillars. The dependency of s is enhanced when the pillar height is relatively large. Different gap sizes make an obvious difference in speed despite of same roughness. For example, the flow parallel to a rectangular array is slower than diagonal directional flow due to the different the gap sizes, as shown in Fig. 3.8(a). Likewise, the hexagonal arrays show different flow speed between longitudinal and transverse imbibition.(Fig. 3.8(b)) Given the pillar dimensions and roughness (h, d, f), maximum gap, $s_{max} \sim \pi h/(f-1)$, allows the flow speed maximized where the structure coefficient $\eta_{max} \approx \frac{f-1}{1+(f-1)^2/(\pi - d(f-1)/h)}$. Consequently, by controlling s, the flow speed can be optimized when the number of pillars are limited on a specific areal substrate.

Our study offers a more accurate but simple theory that is applicable to a wide range of structural properties. Thus, it can provide a reasonable theoretical basis for related fields such as lab-on-a-chip, humidifier, heat pipe or other industries using porous media as a liquid channel. For instance,

this study will provide theoretical basis on analysis of liquid flow in wicks of micro heat pipe, in heat pipe industries and control of the film spreading on porous plates in dehumidifier industries. Furthermore, our scaling laws can contribute toward future studies of liquid imbibition in porous media owing to the simplicity and high accuracy. Multi-porous flow or imbibition within highly complicated structures can benefit from our scaling laws.

Chapter 4

Capillary rise between superhydrophilic substrates

4.1 Introduction

When we vertically place a towel on water surface, water rises up along and inside the towel. And in case of a brick on water puddle, water imbibes up through the tiny gaps between the granules of the brick. These common phenomena are caused by capillary force of water which overwhelms the gravity. The vertical capillary imbibition against gravity is called by capillary rise, which is widely studied for decades. In the studies, various types of channels are employed, such as a cylindrical tube, two parallel rigid smooth surfaces, or single sized micro porous substrates (Dreyer *et al.*, 1994; Levine *et al.*, 1979; Xiao *et al.*, 2010). Unfortunately, most of the phenomena involved in nature and laboratory are not the flow of single sized porous media or along the smooth channel but the flow within multi-porous structures, where considerably complicated analysis to understand the dynamics is demanded. Nevertheless, the detailed analysis of multi-porous media flow at a time is still difficult since substantial amount of stepwise studies are further required for perfect understanding in current level. In this study, as a part of the stepwise studies, we propose one of the simplest

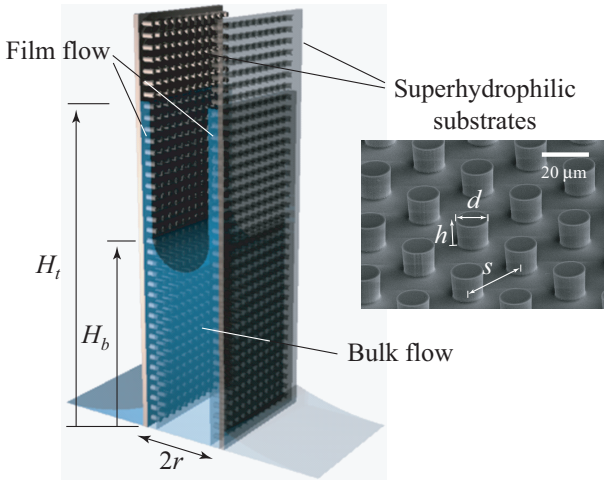

Figure 4.1: Experimental setup for understanding capillary rise of dual porous structures. Two superhydrophilic substrates are used for parallel porous plates on which micro pillar arrays are rectangularly arranged. The scanning electronic microscopy(SEM) image shows the micro structures. Bulk flow occurs at the gap between the walls and film flow occurs above the bulk part.

form of the flow in multi-porous system, capillary rise within parallel superhydrophilic substrates, a dual porous system that involves a millimetric gap between the substrates and ten micrometric pillars of the substrate. We aim to construct scaling laws elucidating the flow within the gap, another flow through the micro structures forming a thin film and the correlation of the two flows and experimentally verify the laws.

4.2 Experiments

The capillary rise within parallel porous substrates was once introduced in 2002 (Bico *et al.*, 2002). But, they proposed the idea without performing further theoretical or experimental approaches. In this work, we prepared an experimental setup, as shown in Fig. 4.1, and performed experiments

	Liquid	γ (N/m)	μ(Pa·s)	ρ(kg/m^3)
A	Glycerine 90 wt%	0.063	0.125	1225
B	Glycerine 85 wt%	0.063	0.086	1213
C	Ethylene glycol solution	0.052	0.062	1168
D	Silicone oil 350 cst	0.020	0.35	970
E	Silicone oil 1000 cst	0.020	1.00	970

Table 4.1: Liquid properties at about 23°C.

in various conditions depending on the porous substrate properties, liquid properties(surface tension and viscosity) and a gap between the substrates. For the porous substrates, we use two parallel superhydrophilic substrates, silicon wafers that are decorated with cylindrical micro pillar arrays that are fabricated by DRIE process, as already used before in other studies (Courbin *et al.*, 2007; Kim *et al.*, 2011a,b). The entire substrate is, additionally, coated with the Si-incorporated diamond-like carbon film to enhance the wettability and the substrate is plasma-etched by air to make the substrate superhydrophilic (Yi *et al.*, 2010).

The pillars are squarely arranged and individually cylindrical with diameter d, height h and pitch (pillar center to center distance) s: $h, d, s \in$[5 40]μm. (See Fig. 4.1) Aqueous glycerine solutions with different concentrations 85 wt% and 90 wt%, ethylene glycol solution with glycerine in the mixing ratio, 60 wt% and 40 wt%, and silicone oils (350cst and 1000cst) are used for deriving the dependency of surface tension and viscosity, which are listed in Table 5.1. And the gap between the parallel plates are in range of [450 1200]μm. The images are taken by a CCD (charge coupled device) and magnification lens with frame rate, [30 60] s^{-1}.

When the end of the substrates gently touch liquid surface, the liquid immediately inflows into the gap between the two substrates. The flow involves two different scales of flow, *bulk flow* and *film flow*. The bulk flow means the flow between the substrates with bulk meniscus as large as

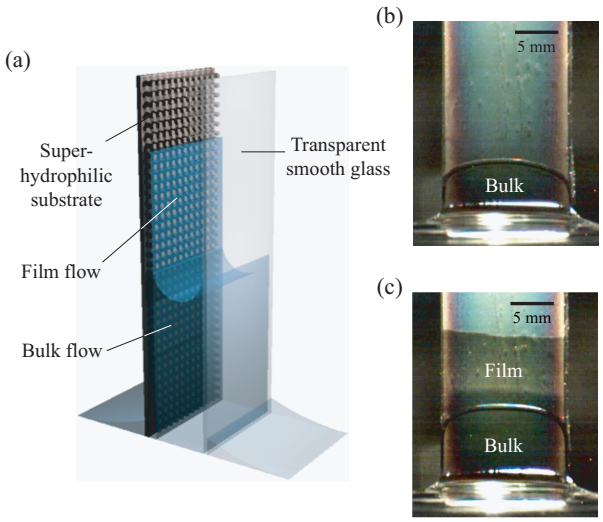

Figure 4.2: (a) Additional experimental setup for clear visualization of the film flow. A transparent smooth glass plate is used for observing film propagation impregnating the micro pillar arrays of the substrate. (b) At the beginning, only bulk flow is observed. (c) Whereas, as the bulk speed decreases, film emanates above the bulk.

the gap size. And the film flow means the flow through the micro pillar arrays on the substrates, forming a thin film of which the thickness is approximately the pillar height, h. For the clear visualization of the film flow, we prepare additional experimental setup, in which a transparent glass plate is used with the superhydrophilic substrate, delineated in Fig. 4.2(a). The transparent glass sheet plate is pre-wetted to sufficiently reduce the contact line singularity. Initially, only bulk flow occurs, whereas, later, film flow starts to emerge from the bulk on the substrates as the bulk flow slows down, hence, both flows eventually occur at the same time. (See Fig. 4.2(b) and (c)) Both of the flows arise due to minimize the surface energy, the capillarity. It is necessary to analyze the kinetics of the flows to construct scaling laws delineating the liquid movements.

4.3 Bulk flow dynamics

In case of the bulk flow, the flow is driven by pressure difference between the bulk meniscus and the entrance due to the capillary pressure drop of the bulk meniscus. The pressure drop, laplace pressure, is approximately evaluated as σ/r with σ and r being surface tension coefficient and half of the gap size, respectively.

Even though the wall substrates have pillars which contribute to increase the pressure drop, the scale of the pressure drop is too small to significantly affect the bulk flow due to the small size of the pillars,($r \gg h$) which gives that the bulk meniscus dominantly drives the bulk flow. So, the driving force, product of pressure and exerted area, is then given by $F_{b,d} \sim \sigma$ in the form of force per unit width. The flow is resisted by gravity and viscous shear force. The gravitational force by the liquid weight is roughly estimated by $F_{b,g} \sim \rho g H_b r$, with H_b being the bulk height as delineated in Fig. 4.1. The viscous shear force is evaluated in a product of shear stress and the area of the walls. Considering the pillar height is too small to resist the bulk flow, the shear stress is approximately scaled

as $\sim \mu U_b/r$ with $U_b = \mathrm{d}H_b/\mathrm{d}t$ and the exerted area is estimated as the projected area of the micro textured wall, not the actual area (Lee & Kim, 2014). Accordingly, the force is scaled as $F_{b,\tau} \sim \mu U_b H_b/r$. The flow is independent of the inertial force, because Reynolds number is much smaller than 1, $Re \sim O(10^{-4})$. So, the total resisting force, sum of the gravitational force and the viscous shear force ($F_{b,g} + F_{b,\tau}$) is balanced with the driving force ($F_{b,d} \sim \sigma$) which gives the governing equation as,

$$\frac{\sigma}{r} \sim \mu \frac{U_b H_b}{r^2} + \rho g H_b. \tag{4.1}$$

As shown in the law (4.1) of bulk flow, there does not exist any term about the micro pillar structure. For verification, we focus on experiments of bulk rise within substrates of different roughnesses, including ideally smooth substrates for comparison. To prevent the contact line singularity, the smooth substrates are pre-wetted before the experiments. Fig. 4.3 represents the experimental results of rough substrate less rough substrate and smooth substrate with a curve using the scaling law (4.1), which shows good agreement between the data points and the theory. The gravitational effect, not significant at the beginning, gradually increases at late time and eventually stops the flow. The final height is expressed as $\approx \sigma/(\rho g r)$, which is the Jurin's height, H_J (Jurin, 1717-1719), which is also consistence with the experimental results in Fig. 4.3. The scaling law (4.1) is identical to the well-known theory, capillary rise between smooth surfaces (Washburn, 1921). Consequently, in spite of existence of the hydrophilic micro pillar arrays on the substrate, the bulk rise of any rough substrates shows almost identical flow behavior as that of smooth pre-wetted substrates with equal gap size.($= 2r$) In other words, the bulk rise is independent of micro pillar configurations only when the pillar is relatively quite small. This result is similar to another study about capillary rise within rectangular tube, combination of bulk rise and interior corner rise in comparatively small

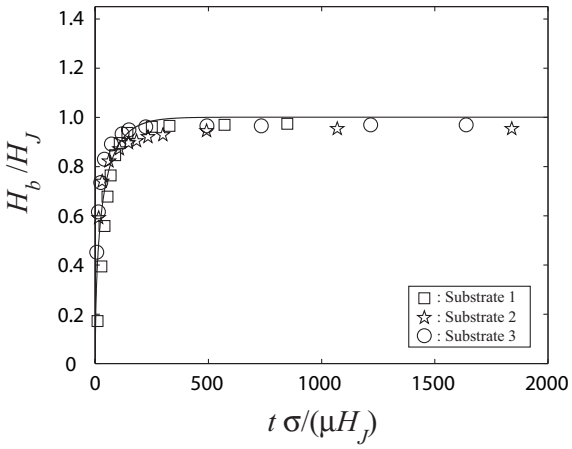

Figure 4.3: Dimensionless form of bulk heights (H_b/H_J) of different substrates, plotted according to the relation (4.1) for same liquid Glycerine 90wt%. Substrate 1 and substrate 2 are a rough substrate and less rough substrate, of which the scale of the micro pillar arrays are [s=40, d=20, h=35]μm and [s=40, d=10, h=2.7]μm, respectively. Substrate 3 is ideally flat substrate pre-wetted by the liquid. As shown in the plot, independent of the micro pillar arrays, the bulk flows show almost identical behavior to that of the smooth pre-wetted substrates. The horizontal line shows the final height, which is almost identical to the Jurin's height for the gap size, r. ($H_b/H_J \approx 1.0$)

scale, where the bulk rise occurs independent of the interior corner rise (Weislogel, 2012).

4.4 Bifurcation point

Before it reaches the Jurin's height, as the bulk flow speed decreases, film starts to deviate from the bulk at a specific point and be shown up on the substrate above the bulk. The point when the liquid becomes to bifurcate is referred to as *bifurcation point*.

The bifurcation occurs at the height where the bulk rise speed (U_b)

(a)

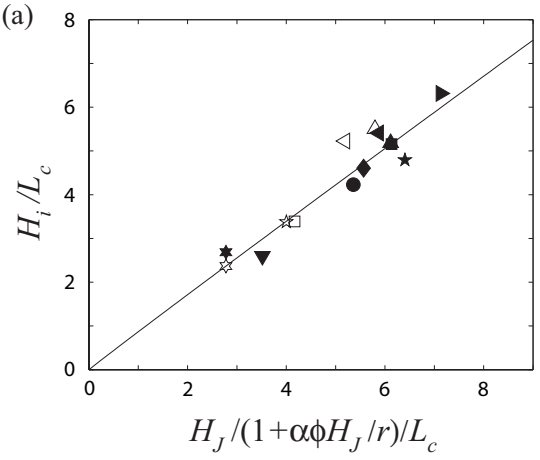

(b)

Symbol	Liquid	Gap (mm)	Substrate (μm)			
			s	*d*	*h*	*f*
●	A	0.6	40	20	35	2.37
◀	A	0.6	40	10	35	1.69
◆	A	0.6	40	20	26	2.02
▲	A	0.6	40	10	26	1.51
△	A	0.45	40	20	35	2.37
■	B	0.6	40	10	26	1.51
◁	C	0.6	40	20	35	2.37
□	A	0.99	40	10	35	1.69
★	D	0.99	40	20	26	2.02
▶	A	0.6	40	20	2.7	1.11
▼	A	1.19	40	20	26	2.02
☆	A	0.99	40	20	35	2.37
✡	E	0.99	40	20	26	2.02
★	A	0.6	40	20	9	1.35

Figure 4.4: (a) Non-dimensional form of bifurcation point using capillary length, $\sqrt{\sigma/\rho g}$, plotted according to the scaling law (4.2). The best fitting line of the data points is approximately $H_i/L_c \approx 0.814(H_J/(1+\alpha\phi H_J/r))^{1.02}$. The experimental conditions, including micro pillar sizes, for each symbol are listed in (b).

becomes to be lower than the initial speed of film rise (U_f). The bulk speed is estimated as $U_b \sim r(\sigma - \rho g H r)/(\mu H)$, derived from the equation (4.1). Unlike the bulk flow, the dynamics of film flow is directly affected by the micro pillar arrays. When considering film flow initiation, we have to concentrate on the precursor film propagation at the front, since the film flow begins by extremely thin film propagation toward dry substrate above. Given the roughness (f), equal to the ratio of the actual solid area and the projected area, the mean pressure drop due to the micro pillar array at the wet front is scaled as $\sim \sigma(f-1)/h$, which is derived by mean surface energy change rate (Srivastava *et al.*, 2010). The pressure difference between the wet front and bulk meniscus is roughly $\sim \sigma((f-1) - h/r)/h$, which is typically $\sim \sigma(f-1)/h$, since $r \ll h$. So, the driving force is scaled as $F_{df,i} \sim \sigma(f-1)$. At the moment when the film starts to emanate from the bulk, there is no liquid film on the substrates above the bulk, thereby dominant shear stress occurs only at the vicinity of the contact line, meaning that the viscous dissipation arises to resist the flow. When the flow is resisted at the precursor film at the front end, contact line singularity take places. To derive the initial film rise speed, U_f, gravitational and inertial forces are neglected, because the scale of the film thickness and imbibition speed are quite small. The shear stress at the precursor film is scaled as $\tau_{f,i} \sim \mu U_{f,i}/(x\theta)$, considering precursor thickness is $h_{f,i} \approx x\theta$ where x is the distance from contact line and θ is the intrinsic contact angle of the substrate, approximately 5°. The exerted area is the entire surface including pillar side area and base area, which roughly gives the area, $f\mathrm{d}x$ in average. So, the resisting force at the precursor film is roughly estimated as $F_{rf,i} \sim \int_\lambda^\Lambda \mu U_{f,i} f/(x\theta)\mathrm{d}x \sim \mu U_{f,i} f \ln(\Lambda/\lambda)/\theta$, where $\Lambda \sim O(10^{-6})$ and $\lambda \sim O(10^{-9})$ are the characteristic extension of the wedge and the cut-off length (order of a molecular size), respectively (de Gennes *et al.*, 2004). Balancing the driving force and dominant resisting force, $F_{df,i} \sim F_{rf,i}$,

the film emerging speed can be derived as $U_{f,i} \sim \sigma\phi\theta/(\mu \ln(\Lambda/\lambda))$, with $\phi = 1 - 1/f$.

By $U_{f,i} \sim U_b$, the bifurcation point can be quantitatively derived. Using a constant $\alpha = \theta/\ln(\Lambda/\lambda) \approx 0.0126$, Jurin's height, and capillary length ($L_c = \sqrt{\sigma/(\rho g)}$), the bifurcation height, H_i, is approximately written in dimensionless form as the following,

$$\frac{H_i}{L_c} \sim \frac{H_J/L_c}{1 + \alpha\phi H_J/r}. \tag{4.2}$$

Fig. 4.4(a) shows that the experimental data points collapse onto a single line. The bifurcation point is directly associated with Jurin's height, which is verified by the scaling law (4.2). For the same Jurin's height, the larger gap size is and the smaller roughness of the porous substrate is, the lower bifurcation point is located. Thus, if the film propagation speed is relatively high, the bifurcation occurs at low height, whereas, if the bulk speed is relatively high, the bifurcation is postponed until the bulk speed becomes to be sufficiently low for the film initiation speed to overwhelm the bulk speed.

4.5 Film flow dynamics

As the bulk height passes the bifurcation point, thin film emerges on the substrate to start to advance ahead of the bulk. During the film flow, gravity does not significantly affect the flow in the range of our interest. ([0 0.07]m) The film spreading, where the distance is measured by the height difference of bulk and film, is separated by two distinct regimes, where the distance is linear to the elapsed time (early stage) and where the distance is proportional to the time to the one-half,(late stage) as shown in Fig. 4.5.

In energetic point of view, as the bulk and the film advance, total surface energy decreases. Simultaneously, gravity and friction due to shear stresses at bulk and film increase the energy of the system meaning that these act

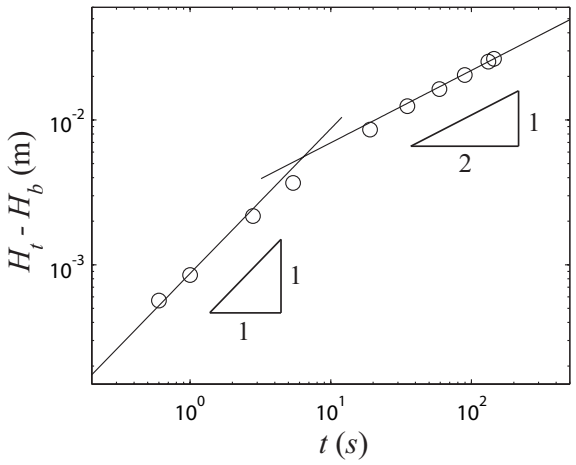

Figure 4.5: The film rise shows mainly two different flow tendencies according to the power law of the film flow dynamics. At moment the film emerges from the bulk, the propagation distance $(H_t - H_b)$ is linearly related to the time duration. However, as the film sufficiently propagates, the propagation distance is eventually proportional to the square root of the time, which represents the classical diffusive behavior.

as energy loss for the flow. Inertia is negligible, since flow speed everywhere is generally not sufficiently fast. The surface energy change rate is written as sum of $\sim -\sigma \mathrm{d}H_b$ for the bulk and $\sim -\sigma(f-1)\mathrm{d}H_t$ for the film, where H_t means the total height and is film height when film exists. The rate for gravity is $\sim \rho g H_b r \mathrm{d}H_b$. The friction loss occurs at both of the bulk and the thin film, meaning that as the liquid is supplied through the bulk for the film flow, viscous shear force is generated at the bulk as well as the film. The shear forces of the both flows are evaluated as products of shear force and the exerted area in bulk and film parts.

To derive the dominant shear force, viscous dissipation should also be considered to be estimated and compared with other shear forces. Given the wedge speed, U_w, the shear force at the wedge is scaled as $\sim \mu U_w f \ln(\Lambda/\lambda)/\theta$, as already derived. When film flow exists unlike the initiation, we assume the speed of the wedge of which height is h_w is roughly estimated as the flow speed at the same height (h_w) in the film, $U_w \sim U_t(h_w/h)$, with U_t being film advance speed. So, the viscous shear force due to the viscous dissipation at the wedge is scaled as $F_{r,w} \sim \mu U_t h_w ln(\Lambda/\lambda)/(h\theta)$. The shear force generated at the film is roughly $\sim \mu U_t(H_t - H_b)/h$ which is typically greater than the $F_{r,w}$, because the shear force ratio of contact line singularity(viscous dissipation) and the film is less than 10^{-1} for $H_t - H_b > 10^{-4}$m. Thus, the flow is not significantly affected by the viscous dissipation any longer except the initiation.

Using the dimensionless parameter, $\zeta = 1 + h(f-1)/w$ with $w = s - d$, the surface energy change rates above are estimated as $\sim \mu U H_b \mathrm{d}H_b/r$ and $\sim \zeta \mu U_t(H_t - H_b)\mathrm{d}(H_t - H_b)/h$, where U and $U_t = \mathrm{d}H_t/\mathrm{d}t$ are the average speeds of the bulk and the film propagation speed, respectively (Kim *et al.*, 2015). Thus, the energy change rate for the whole system is roughly estimated as,

$$\sigma(1+(f-1)\frac{U_t}{U_b}) \sim \rho g H_b r + \rho g (H_t - H_b)h + \mu \frac{U H_b}{r} + \mu\zeta \frac{H_t - H_b}{h}(U_t - U_b)\frac{U_t}{U_b}. \tag{4.3}$$

The scaling law (4.3) is a universal relation describing the dynamics of bulk and film rise. The volume conservation, $2U(r+h) \approx 2rU_b + hU_t$ gives $U \approx U_b + h(U_t - U_b)/r$, because $r \gg h$. Moreover, in this height range $H_t \in$ [0 70] mm, the gravity term, $\rho g(H_t - H_b)h$ is neglected for $r \gg h$. Before the film emanates, H_t is equal to H_b, which gives the relation (4.3) being the bulk relation (4.1). Using the volume conservation and subtracting the bulk relation (4.1)from the scaling law (4.3), the film propagation dynamics is written in the following form,

$$\sigma(f-1)\frac{U_t}{U_b} \sim \mu \frac{(U_t - U_b)H_b h}{r^2} + \mu\zeta \frac{H_t - H_b}{h}(U_t - U_b)\frac{U_t}{U_b}. \tag{4.4}$$

4.5.1 Early stages

At the very beginning of the film emergence, the film propagation distance, less than $O(100)\mu m$, is so small that the shear force exerted on the film is also small. At this time, the shear stress at the bulk for providing liquid to the film rise is larger than the film shear stress. Thus, considering $H_b \sim H_i$ with $(U_t - U_b)/U_t \ll 1$, the relative film speed, $U_t - U_b$ from the scaling law (4.4) is scaled as $U_t - U_b \sim \sigma(f-1)r^2/(\mu H_i h)$, which gives the relation of $H_t - H_b$,

$$H_t - H_b \sim \frac{\sigma}{\mu}(f-1)\frac{r^2}{H_i h}t \tag{4.5}$$

where t means the elapsed time from when the film begins to emerge from the bulk. Fig.4.4 shows the experimental results with the line indicating scaling law (4.5). The experimental data points are collapsed on the line but gradually diverge from the line, as the film further propagates, since the scaling law is valid only when it is very early stage. In this point of

view, this law in the plot (4.6) can be considered an asymptotic relation. The linear region is so early that the contact line singularity enables to significantly affect the overall resisting force. For the data points of Fig. 4.6, the shear force ratios of viscous dissipation at the contact line and bulk are typically less than 0.1;hence, the viscous dissipation is considered to be neglected.

If the bifurcation point is located at a higher position, the region where bulk shear force is larger than the film shear force becomes larger, which gives the linear regime larger. And in spite of the same bifurcation point, if the gap is smaller, linear regime is larger, too. This law shows the different power law response from the diffusive power law, $L \propto t^{1/2}$, classical Washburn's law, with L and t being wicking distance and time duration, respectively. For the liquid flow through a cylindrical channel with constant width or single sized porous media, such as uniformly arranged micro pillar array substrate or glass bead pack, the liquid flows inevitably follow the Washburn's law, since the mean laplace pressure and mean shear stress are entirely constant. Whereas, for the multi-sized porous media, variation of the channel size changes the dominant laplace pressure and shear stress, which enables to show unusual power laws and the linearity of the law (4.5) is one of the cases.

4.5.2 Late stages

In the late stage when the film propagates more than before, ($H_t - H_b > O(10^{-3})$m) the area where film spans becomes large. Accordingly, the shear force at the film becomes large so that the film shear force is the dominant shear force. Compared with the shear force of film, viscous friction for providing liquid to film rise is negligibly small. In this case, the bulk part acts as a liquid reservoir. Neglecting the viscous term of the bulk, the modified scaling law from the preceding relation (4.4) gives the relative speed of film flow as $U_t - U_b \sim \sigma\eta h/(\mu(H_t - H_b))$, with $\eta =$

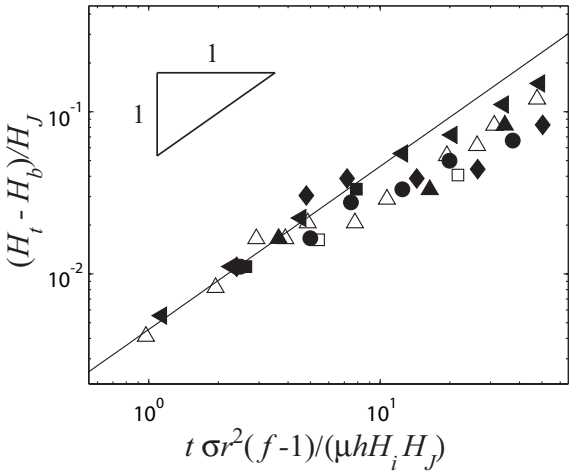

Figure 4.6: Evolution of scaled film advancing distance as a function of the time based on the scaling law (4.5). The linear relation of the law (4.5) is an asymptotic line for the beginning, which shows good agreement with the experimental results, at first, whereas the data points gradually diverge from the line (index=1) toward the direction of diminishing the index, as the time elapses. The slope for best fitting line is 1.01 with the standard deviation of 0.059 when the initiation. The experimental conditions for symbols are listed in Fig. 4.4(b).

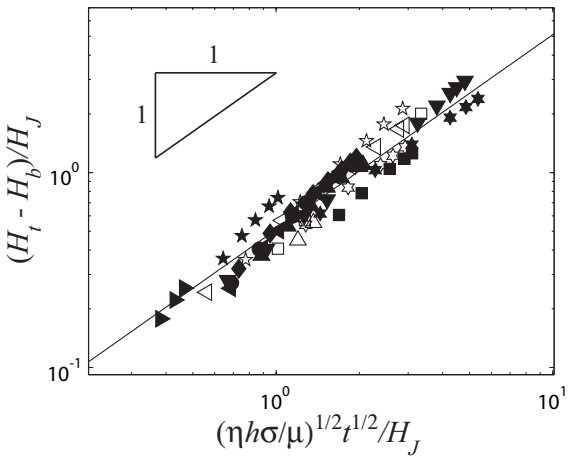

Figure 4.7: Scaled film advancing distance plotted according to the scaling law (4.6). Unlike the early stage, the dominant friction occurs at the film, which gives the distance proportional to square root of the time. In the plot, the slope for best fitting line is 1.05 with the standard deviation of 0.031 for the late stages. The experimental conditions for symbols are listed in Fig. 4.4(b).

$(f-1)/[1+h(f-1)/w]$. Integrating this equation, the relation of the thin film length $H_t - H_b$ is derived as follows,

$$H_t - H_b \sim (\eta\frac{\sigma}{\mu}h)^{1/2}t^{1/2}. \tag{4.6}$$

The line from this law (4.6) is another asymptotic line and the data points converge to the line as the film propagates. Fig. 4.7 shows good agreement between the experimental results for the late stage and the equation (4.6). The film rise of late stage that shows the Washburn's dynamics is not significantly different from the hemi-wicking rise on a single superhydrophilic wall(Kim *et al.*, 2015). As shown in the scaling law (4.6) and the plot in Fig. 4.7, substrate gap does not seriously affect the film flow, eventually.

4.5.3 Conclusions

In conclusion, we have experimentally and theoretically studied the dynamics of the liquid imbibition into parallel micro porous substrates. The flow involves the bulk flow at the millimetric gap and the film flow in the micrometric pores above the bulk. We have presented scaling laws for the bulk flow within the gap between the substrates and film flow through the micro pillar arrays partially associated with the bulk flow. The bulk flow shows identical behavior to what is observed on smooth substrates, implying that the bulk flow is independent of the microstructures. The film flow is affected by the bulk in the beginning, whereas the film flow becomes independent of the bulk flow in the late stages. Moreover, the film emanating height ahead of the bulk part has been investigated by comparing the rising speeds of bulk and film. Consequently, the current work quantitatively clarifies the mechanism of the flow into dual porous media by accounting for the individual flows into large pore and small pore including the correlations. Thus, we found out some information of fundamental characteristics

of the flow in porous media, i.e. which pores play important role to drive a specific flow or magnitude of dominant resisting forces.

Considering most of the porous structures are characterized by combination of different length scales, this study can be a starting point to understand the flow in multi-porous media, where complicated analysis is required. In various industrial fields, such as lab-on-a-chip or HVAC (heating, ventilation and air-conditioning) industries, our work will provide theoretical basis to approach a number of the porous media flow problems awaiting reasonable modeling and quantitative experiments. Also, it can experimentally and theoretically support to fundamental analysis of biological phenomena and additional studies addressing other effects such as swelling or elastocapillarity, in academic fields.

Chapter 5

Hydrodynamics of capillary imbibition in cellulose sponges

5.1 Introduction

A number of materials in the earth have plenty of various pores, such as xylem of trees, skin of animals, or some igneous rocks. When these materials are faced with chemically attractive liquid, the liquid spontaneously immediately moves into the pores, driven by surface tension, mutual interaction of molecules at the interface, what is called capillarity. Physics of the capillary flow has been applied in numerous jobs of our daily lives for more than thousands of years, for example, historical drawings or writings by absorbing ink into pores formed by fibers of papers, oil dampened paper as windows in traditional Korean construction, oil infiltration into wooden instrument to prevent deformation, and cleaning process by absorbing aqueous liquid in fabrics of towel or tissue. Recently, owing to microminiaturization of machines and development of fabrication technologies, capillarity has involved more widely in many fields of industries such as heat pipe, dehumidifier or lab-on-a-chip industries related to micro, nano-

and bio-technology. Thus, highly sophisticated prediction and control of flow are required for optimization, hence the capillary imbibition in porous media has been intensively studied for last decades.

To understand the physics of capillary imbibition, uniformly arranged porous structures were used to alleviate the difficulties for an accurate analysis of the flow in inherently complex and irregular porous structures. For 2-D flow, a plate with micro pillar arrays is used as a simplified porous structure for observing particular liquid wetting behavior (Courbin *et al.*, 2007) and constructing scaling laws (Ishino *et al.*, 2007; Kim *et al.*, 2011a,b). Numerical analysis also has been performed to describe the flow more exactly (Srivastava *et al.*, 2010; Xiao *et al.*, 2010). For 3-D flow, various sized glass beads were used to form tiny spaces where liquid flow occurs, especially in soil science (Delker *et al.*, 1996; Lago & Araujo, 2001). Also, water absorption into floating objects was studied by experimental and numerical analysis (Vella & Huppert, 2007). Most of the studies are characterized in classical Washburn's dynamics ($x \propto t^{1/2}$), whereas different scaling law, $x \sim t^{1/3}$, has been proposed by introducing corner flow dynamics (Ponomarenko *et al.*, 2011; Weislogel, 2012).

However, in spite of the studies above, further studies addressing multi-sized porous media is still required to analyze liquid imbibition in various cases of nature and industries. Here, using cellulose sponges, typically thought as multi-porous media, we have performed experimental and theoretical studies of capillary rise into 3-D porous media. For understanding flow dynamics in sponge more accurately, we first start with the horizontal imbibition to quantify the liquid spreading dynamics without gravity. And we address the vertical imbibition to elucidate the dynamics under gravitational effect using the results of horizontal imbibition. Through the entire works, we aim to construct scaling laws for the horizontal and vertical imbibition dynamics and experimentally corroborate the simplified model to rationalize the physics of liquid imbibition in multi-sized porous structures.

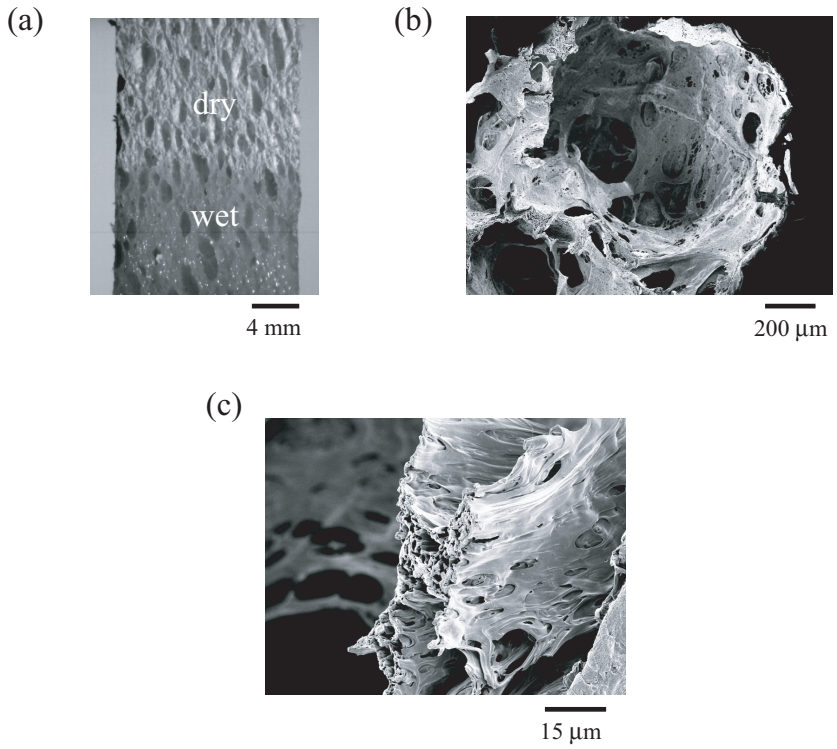

Figure 5.1: : (a) Image of liquid imbibition with wet-dry interface in cellulose sponge. (b) Scanning electron microscopy (SEM) image of large void in which many holes are existed on the wall as channels toward the next large void. (c) Cross sectional image of the porous wall.

5.2 Sponge model and experimental setup

To elucidate the liquid behavior infiltrating into sponges, structural analysis of pores in sponge should be preceded. As shown in magnified images in Fig. 5.1(a), there are plenty of various sized pores where liquid can flow inside or stay statically leaning on pore walls. The characteristics of pores are highly associated the manufacturing process of sponge. Sponge is made from mixture of shredded cellulose sheets and sodium sulphate crystals. The mixture, which is referred to as *viscose*, is heated to melt

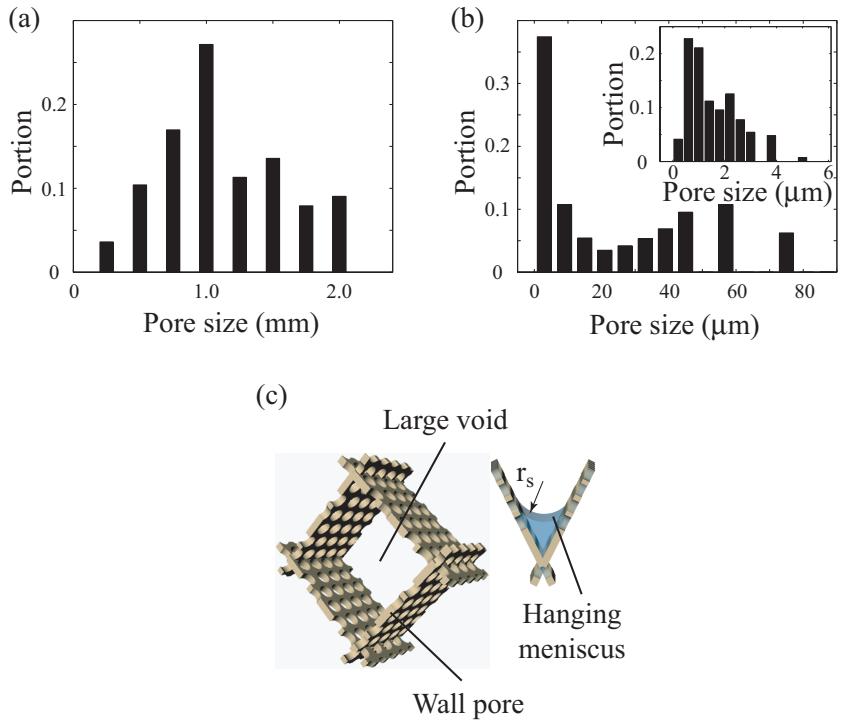

Figure 5.2: : Characteristics of pores in sponge and simplified model of a unit pore. (a) Bar chart of large void distribution plotted with pore size(mm) and volumetric portion of each pore. The portion is derived as the average portion of the length occupied by each pore, given randomly selected lines. Most of the pores are distributed around 1 millimeter. (b) Bar chart of wall pores plotted with pore size(μm) and volumetric portion of each pore. The inset shows detailed distribution of the wall pore size of the first bar, (0 - 6 μm), where majority of the wall pores are distributed in the size of approximately 1 micro meter. (c) A unit simplified model of sponge pore structure. Sponge consists of millimetric large voids and micrometric wall pores.

the crystals and drain the molten liquid away, which eventually forms the ellipsoidal millimetric hole with cellulose wall structures in sponge.

Accordingly, there exist two important different sized pores in sponge, one is the millimetric pore and another one is the micrometric pore inside of the wall, surrounding the large pore. The pores are referred to as *large void* and *wall pore*, respectively (Märtson *et al.*, 1999), which are shown in Fig. 5.1(b) and (c). Bar charts in Fig. 5.2(a) and (b), which show the pore size distributions of large void and wall pore, delineate that the pore sizes are approximately order of 1 millimeter and 1 micro meter, respectively. The Jurin's height of the wall pore is much larger than our experimental range, 10 cm (Jurin, 1717-1719); thus, we assume that the liquid saturates whole wall pores while the imbibition occurs within our interest. Beside of the large voids and wall pores, a partially saturated space encircled by a group of small pores and liquid - air interface can be another type of pore in multi-scale porous system. So, the pores in sponge are widely ranged in size, from order of hundred nanometers to order of millimeters. In this study, by employing a simplified conceptual model of sponge in Fig. 5.2(c), we mainly deal with large voids, wall pores, and additional pores combined with the meniscus hanging against gravity at the edge and a group of adjacent small pores of walls, referred to as *hanging meniscus*.

We used Ethylene glycol 99 wt%, turpentine, and four different kinds of silicone oils (10, 100, 350, and 1000 cst) for parametric analysis of liquid properties listed in the table of supplemental material 5.1. In rheology, all liquids are Newtonian fluids so that we can estimate the exerted shear stress as a product of the viscosity and shear rate. The imbibitions are assumed to be incompressible flow and no slip boundary condition is used for theoretical approaches.

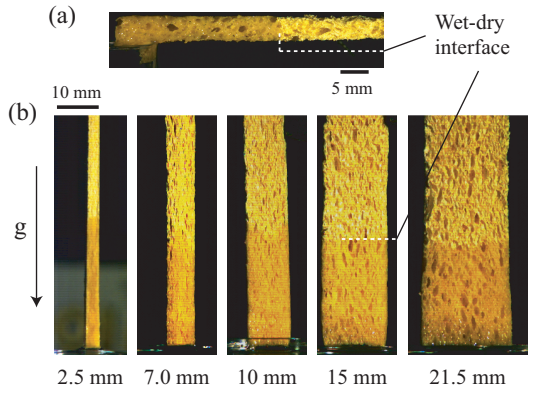

Figure 5.3: : Experimental images of capillary imbibition into sponges. Images of horizontal spreading (a) and vertical spreading (b) of silicone oil with wet-dry interfaces. In case of vertical imbibition, differently pressed sponges are used to deduce the gravitational dependency.

5.3 Horizontal imbibition

We, first, perform experiments for horizontal flow by using sponge bars cut in about 5 mm high, 5 mm thick(perpendicular direction to the paper), and more than 10 cm long as shown in Fig. 5.3(a) which is captured by high speed camera and magnified lens. One end of the bar is protruding downward in approximately 2 mm so that it can absorb and provide liquid horizontally from the reservoir. The protruding part has to be immersed rapidly to reduce the time for liquid to rise up until it reaches to horizontal bar. The lower part of the bar where the liquid has first reached is focused on for measuring time duration and the horizontal distance from the reservoir to wet-dry interface.

Wetting state is more stable energetically than dry state since cellulosic material of sponge is hydrophilic and, moreover, a number of grooves in sponge intensify the hydrophilicity by enlarging the substrate area (Kim *et al.*, 2011a). Thus, at the moment the sponge contacts with liquid in the vessel, the liquid is spontaneously infiltrated by the densely arranged

structures due to affinity of liquid and substrate, which generates capillary pressure drop due to the laplace pressure (Young, 1805). The pressure drop is proportional to principal curvature of liquid surface, which is roughly inversely proportional to the pore size since the contact angle is assumed to be zero. Gravity is assumed to be negligible since the pressure drop overwhelms hydrostatic pressure in horizontal flow, and thereby liquid moves saturating each of the whole sized pores individually.

The flow dynamics is evaluated by considering driving pressure and dominant shear stress that resists the flow. However, the flow resistance in sponge cannot be exactly estimated, due to the structural complexity. So, employing permeability, the transmission ability of fluid by which the resistance is deduced, Darcy's law is used as follows (Darcy, 1961),

$$U_h = -\frac{k}{\mu}\frac{\mathrm{d}p}{\mathrm{d}z} \tag{5.1}$$

where U_h, k, and μ stand for horizontal flow velocity, permeability, and viscosity of liquid, respectively. In porous media, the permeability is proportional to square of pore size,(Millington & Quirk, 1961). This law is established upon the assumption of Newtonian flow.

While small pores surrounding a large pore are consecutively being filled, the larger pore is also being filled. We remark that the flow dominantly occurs through the large pore rather than through the small pores to minimize the exerted shear stress, inversely proportional to cubic of the pore size for the same flow rate. Accordingly, the flow occurs through large possible pores, the large voids, which leads the permeability $k \sim D_0^2$. As a result, how fast the liquid flows through large voids determines the entire interface propagation speed. Wall pores instantly absorbs liquid from the large voids, which we measure as the wet-dry interface. Thus, the driving pressure in horizontal imbibition is roughly estimated as $\sim \sigma/D_0$, driving pressure of filling a large void.

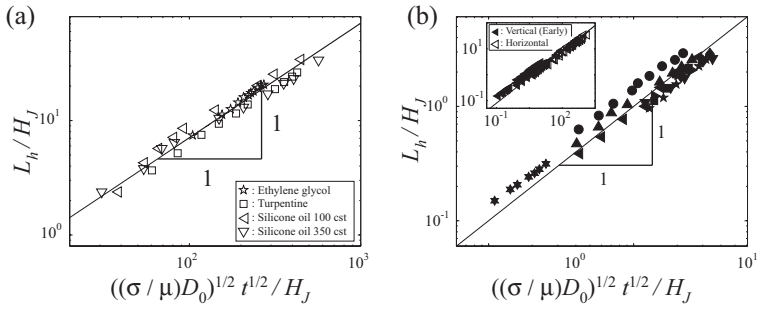

Figure 5.4: : Experimentally measured data points with lines of scaling laws. (a) The scaled horizontal distance (L_h/H_J) plotted according to the scaling law (5.2) (b) Plot of scaling law (5.3) which describes dynamics of the vertical liquid imbibition in early stage. The experimental conditions for each symbol are listed in Fig. 5.5. The flow shows almost same characteristics as the horizontal flow, which results the experimental data of both cases are consistent onto a single line by using the same scaling law (5.2).(inset)

Considering the pressure drop, the pressure term is scaled as $\mathrm{d}p/\mathrm{d}z \sim (\sigma/D_0)/L_h$, with L_h being the horizontal imbibition distance from the starting point. Using the permeability and the pressure term, the flow velocity, $U_h = \mathrm{d}L_h/\mathrm{d}t$, is derived by Darcy's law (5.1), $U_h \sim D_0\sigma/\mu/L_h$. Integrating this relation and using Jurin's height, $H_J \sim \sigma/(\rho g D_0)$, we derive a dimensionless form of the relation between horizontal propagation distance and time as

$$L_h/H_J \sim (D_0\frac{\sigma}{\mu})^{1/2}t^{1/2}/H_J. \tag{5.2}$$

As shown in Fig. 5.4, the experimental data collapse onto one line of the scaling law (5.2). We thus see that liquid propagates with Washburn's law (Washburn, 1921), where the spreading rate depends on the dominant flow channel sizes, D_0 in addition to the classically known prefactor σ/μ. If the large pore is far away from the group of small pores, liquid does not

flow dominantly through the large voids. But, the large voids are usually adjacent to the wall pores as we observe in the Fig. 5.1(a).

5.4 Vertical imbibition

5.4.1 Early stages

Now, we consider how liquids vertically rise along the sponge against gravity. We use pressed sponges whose height and thickness are commonly about 10 cm and 5 mm, respectively, but width ranges 2.5 mm to 21.0 mm as shown in Fig. 5.3(b). To make pressed sponges in different level, sponges are fully wetted by water first so that the shape can be flexibly changed. The sponges are then perfectly dried in the frames of different widths, left at oven of $60°C$ more than 2 hours. The sponge of 2.5 mm width is a maximally pressed one and 21.0 mm wide sponge is unpressed one. When a sponge is pressed, deformation of large voids occurs more dominantly than that of wall pores due to the pore scale difference. Assuming a pore being stack of thin band typed rings, we know pore width change of large void is remarkably easier than wall pores under same exerted pressure (Yang & Kim, 2012). By considering that large voids occupy entire volume of the sponge, the eventual pore size change pore size is roughly linearized by the sponge width change. Unlike the horizontal case, the size of large void (D_0) in vertical case can be varied as the width change. Using linear approximation, the large void size of pressed width is written as $D_0 \approx D_{min} + (D_{max} - D_{min})(w - w_{min})/(w_{max} - w_{min})$ where D_{min}, D_{max}, w_{min}, and w_{max} stand for maximally pressed large void size ($D_{min} \approx 20mu$m), unpressed large void size ($D_{max} \approx 1$ mm), maximally pressed width ($w_{min} \approx 2.5$ mm), and unpressed width ($w_{max} \approx 21$ mm), respectively.

At the moment vertically erected sponge block comes to the liquid surface, the liquid immediately infiltrates through the pores likewise, but, the

entire liquid movement shows quite different tendency. The rise speed of the initial stage is relatively high, however, at the late stage the speed dramatically lowers down. At the beginning, flow shows same dynamics as the horizontal imbibition. Whole pores are also fully saturated because the liquid position is still low so that the laplace pressure dominates the hydrostatic pressure even at the large voids. Liquid also moves through the large voids, which leads the permeability, $k \sim D_0^2$. Likewise, the pressure gradient is the same, $\mathrm{d}p/\mathrm{d}z \sim (\sigma/D_0)/H_v$, with H_v being the vertical height. Thus, by using Jurin's height, the dynamics of vertical rise of early stage is written in dimensionless form as,

$$H_v/H_J \sim (D_0\frac{\sigma}{\mu})^{1/2}t^{1/2}/H_J. \tag{5.3}$$

The experimental data are entirely consistent onto the scaling law (5.3) as shown in Fig. 5.4(b). The inset of the Fig. 5.4(b) demonstrates that the dynamics of the horizontal flow and the early stage of the vertical flow are almost identical. In both of the cases, all pores are completely saturated by the liquid, which is referred to as *complete filling* that is shown in Fig. 5.6(a). When *complete filling* occurs, even though the wet-dry interface propagates, macroscopic surface energy change rate at the front part is approximately constant as well as dominant shear stress is constant along the liquid path. So, the driving force is independent of the spreading distance and the resisting force is proportional to the distance, which leads to a diffusive rule for the distance $L \propto t^{1/2}$. Considering the proportional factor forms $a\sigma/\mu$, with a being length scale, we remark that the *complete filling* yields to Washburn's law (Washburn, 1921).

5.4.2 Late stages

As the height increases more, gravitational force does not allow whole sized pores to be saturated, since the capillary forces generated at whole sized pores do not always overwhelm the gravitational force. Considering

gravity, the pressure gradient that drives the flow is estimated approximately as $\sim \sigma/(rH_v) - \rho g$ with r being a pore radius. The gravity at the pore cannot be neglected unless the pore radius is sufficient small so that $\sigma/(rH_v) \gg \rho g$. The maximum size of saturated pore is derived as $r_s \sim \sigma/(\rho g H_v)$ at a specific height, H_v (Obara & Okumura, 2012), which means every pore smaller than r_s is absolutely filled. Moreover, if some of the small saturated pores are adjacent, the space surrounded by the plural small pores can have additional liquid bulk with the liquid-air surface of r_s, as illustrated in Fig. 5.2(c), for minimizing surface area to form a meniscus at the edges (hanging meniscus). Consequently, large voids cannot be completely filled due to gravity but partially filled; thus, this is referred to as *partial filling*. Imbibition characteristic of the *partial filling* is simply described in Fig. 5.6.

When *partial filling* occurs, the pressure drop of the meniscus hanging at edge of the vicinity of the wet-dry interface cannot additionally drive the flow. This is because the radius of surface curvature is invariably r_s, irrespective of size of the pore at the hanging meniscus, and the pressure drop is invariably balanced with hydrostatic pressure. Thus, the driving pressure of *partial filling* is generated by wall pores and is independent of hydrostatic pressure, since Bond number which is ratio of gravitational force and capillary force is much smaller than 1, $\rho g(H_v r_p)/\sigma \sim O(10^{-2}) \ll 1$. Consequently, the pressure gradient of *partial filling* of the Darcy's law is scaled as $\mathrm{d}p/\mathrm{d}z \sim (\sigma/r_p)/H_v$, while that of *complete filling* is $\sim (\sigma/D_0)/H_v$, associated with large void.

To evaluate the driving pressure of *partial filling*, (σ/r_p), the wall pore size is necessary to be examined. An additional experiment of pressed sponge is performed for liquid infiltration into pure wall pore structure without large voids. To make the pressed sponge, a sponge between parallel blocks is perfectly wetted by water for softening the dry cellulose structure. The sponge is then pressed by the blocks in approximately $3.7 \times 10^5 N/m^2$

and dried in the oven (60 $^{\circ}C$ more than 24 hours). The sponge was originally 25 mm thick before being wet, but the eventual thickness is 2.75 mm. As shown in Fig. 5.7(a), when the sponge binding with the blocks touches liquid surface,(Silicone oil 10cst) the liquid rises saturating the entire pores, which is classified in *complete filling*.(See Fig. 5.7(b)) This is because the pore size (much smaller than $O(100\mu\text{m})$) is so small that the laplace pressure is large enough to ignore gravity. So, the distance is scaled as $H_{(p)} \sim ((\sigma/\mu)r_{pressed}t)^{1/2}$, with $r_{pressed}$ being an effective pore size. By the experiments, the effective pore size can be derived empirically, which is approximately scaled as $\text{O}(1\mu\text{m})$. While the sponge is pressed sufficiently, the space between walls is almost eliminated, for which we assume that the pressed sponge is pure bulk of porous wall structures only; thus, $r_p \sim r_{pressed}$. Hence, the wall pore size (r_p) is estimated as $r_p \approx O(1\mu m)$, which is also verified by the pore size distribution in Fig. 5.2(b).

In case of *partial filling*, permeability is associated with the size of the hanging meniscus, which decreases as the height increases. The pore size beneath the hanging meniscus (r_g) about height is approximately proportional to the radius of surface curvature, $r_g \propto r_s$. Furthermore, when the sponge block is pressed, r_g is also changed.

As a sponge block is compressed, large voids are dominantly deformed, which determines the channel size of hanging meniscus. The channel size is inversely proportional to the shear stress when the liquid flows; thus, the channel size change rate, $\zeta = D_0/D_{max}$ should be investigated. According to the schematic model in Fig. 5.8, the deformed width (D_0) is roughly scaled as $\sim D_{max} \tan\alpha_2 / \tan\alpha_1$. The wetted lengths by bulk liquid of the two cases are $l_{w1} = r_s/\tan\alpha_1$ and $l_{w2} = r_s/\tan\alpha_2$, respectively. The channel size change rate is roughly scaled as $\zeta \sim l_{w2}/l_{w1}$, which leads $\zeta \sim D_{max}/D_0$. In the same principle, the hanging meniscus is approximately $r_g \sim (D_{max}/D_0)r_s$. The cross sectional area beneath the hanging meniscus is usually larger than the wall pores; thus, the flow

occurs through the consecutive pores of hanging meniscus. So, the permeability is scaled as, $k \sim ((D_{max}/D_0)r_s)^2$ (Dong & Chatzis, 1995), which gives $k \sim \zeta^2\sigma^2/(\rho g H_v)^2$, with $\zeta = D_{max}/D_0$. Substituting the permeability into the Darcy's law (5.1), we derive a relation of the flow speed as $U_v \sim \zeta^2(\sigma^3/\mu)/(r_p(\rho g)^2)/H_v^3$. Integrating the velocity relation about the elapsed time, we find a scaling law of late time imbibition dynamics in dimensionless form as follows,

$$H_v/H_J \sim (\frac{(\rho g)^2}{\sigma\mu}\frac{D_0^2 D_{max}^2}{r_p})^{1/4} t^{1/4}. \tag{5.4}$$

The scaling law (5.4) is an asymptotic line, since it is established when $H_{cri}^4 \ll H_v^4$ is assumed with H_{cri} being the boundary height of *complete filling* and *partial filling*. So, the dispersed data points for different widths are gradually closer to the line of scaling law and finally entirely consistent onto our scaling law (5.4) in Fig. 5.9. Moreover, the Fig. 5.9 shows the boundary height of *complete filling* and *partial filling* by the scaling law, $H_{cri} \sim \sigma/(\rho g D_0)$, which also shows good agreement with the experimental data point. This result indicates that *complete filling* and *partial filling* are determined by whether large void is completely saturated or not.

As we mentioned above, the wall pore size r_p is approximately 1 μm, which means that the size of the large possible pore neglecting gravity is similar to 1 μm. This is same principle that the driving pressure of *complete filling* is approximately σ/D_0. Due to the shear stress minimization, the maximum pore is leading pore of the infiltration. As the height extremely increases, more than 10 m, the wall pore will be partially saturated as the large voids do in this experiments. Then, smaller pore, nano-metric pores, will also take the same role as the wall pore do and it will again be partially saturated in higher location. This regulation is similar to structure of fractal in mathematics, which is one of the rules in nature.

5.4.3 Conclusions

In summary, we have constructed the scaling laws to describe the dynamics of the horizontal and the vertical imbibition of different liquids into various cellulosic sponges, and corroborated the results using experiments. Unlike single sized porous media, multi-sized porous media, sponge, shows different flow mechanics when against gravity, since the pores are selectively saturated by gravity, which gives the unusual result, $H_v \propto t^{1/4}$, different from the classical Washburn's rule, $L \propto t^{1/2}$. The imbibition is classified in two different flow types by whether entire pores are completely saturated or not. Through the entire process of the works of this chapter, we found out some information of fundamental characteristics of the flow in multi sized porous media, i.e. which pores dominantly drives the flows when complete filling and partial filling, magnitude of dominant resisting forces, or uniformity of the permeability.

Although our study focused on capillary spreading on cellulosic sponges with various liquids, not all liquids are predictable, but water or diluted aqueous solutions are excluded. Water spreading on cellulose structure involves chemical adhesion between water and cellulose molecules and swelling effects as well. Those phenomena complicate the physics, thus, this subject should be further pursued in the future. The current work can be a starting point to more accurately understand the flow dynamics inside of the complicated porous structures. Introducing the correlation of bulk flow and film flow, our theories will provide theoretical basis to applications of studies of paper-based microfluidics and micro nano bio-fluidics or other studies to understand natural absorptions (Martinez *et al.*, 2008; Wheeler & Stroock, 2008).

	Liquid	γ (N/m)	μ(Pa·s)	ρ(kg/m^3)
A	Turpentine	0.027	0.0014	870
B	Ethylene Glycol 99 wt%	0.048	0.018	1112
C	Silicone oil 1000 cst	0.020	1.00	970
D	Silicone oil 350 cst	0.020	0.35	970
E	Silicone oil 100 cst	0.020	0.10	970
F	Silicone oil 10 cst	0.020	0.01	970

Table 5.1: Liquid properties at about 23°C.

Complete filling			Partial filling		
Symbol	Liquid	$\frac{w}{w_{max}}$	Symbol	Liquid	$\frac{w}{w_{max}}$
■	A	1	□	A	1
★	B	1	☆	B	1
◀	C	1	◁	C	1
▼	E	1	▽	E	1
◆	F	1	◇	F	1
▶	F	0.71	▷	F	0.71
▲	F	0.48	△	F	0.48
●	F	0.33	○	F	0.33
✸	F	0.12			

Figure 5.5: : Experimental conditions for the symbols of vertical imbibition. The experiments have been performed for different liquids into sponges of differently compressed widths. The degree of compression is directly associated with the width of large voids in sponge.

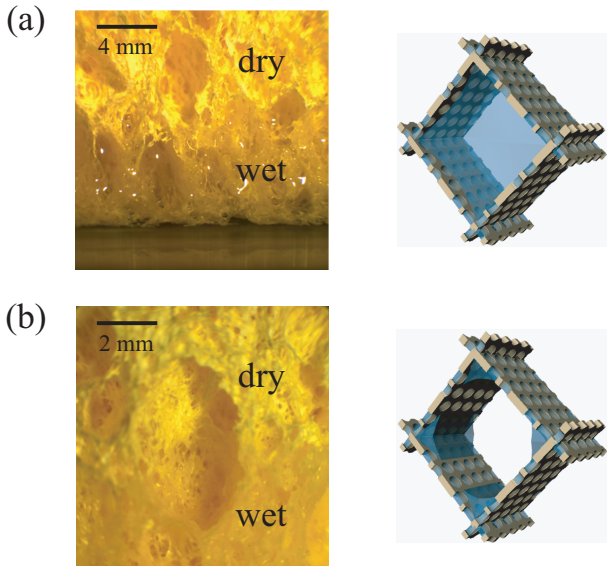

Figure 5.6: : Experimental images and conceptual models. (a) When *complete filling* occurs, wet part is entirely saturated with liquids. In this case, gravity is negligible due to large laplace pressure even in the large voids. (b) When *Partial filling.* occurs, large voids cannot be completely saturated due to large gravitational effect, but part of the large voids and wall pores are saturated.

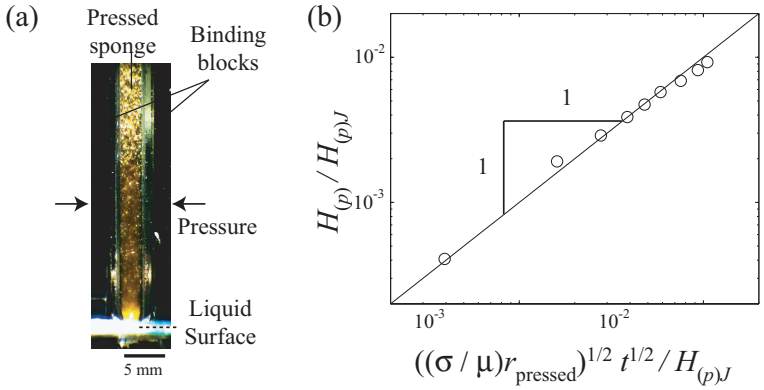

Figure 5.7: : Additional experiments for deduction of wall pore size. (a) Experimental image of liquid imbibition in a pressed sponge. The liquid flow occurs through pores of the pressed sponge between the binding blocks. (b) Plot of scaling law (3) in dimensionless form by using Jurin's height, $H_{(p)J} = \sigma/(\rho g r_{pressed})$. The effective pore size ($r_{pressed}$) is approximately 0.7μm under the assumption of *complete filling* regime, since the pore size is considerably small to be filled, irrespective of gravity.

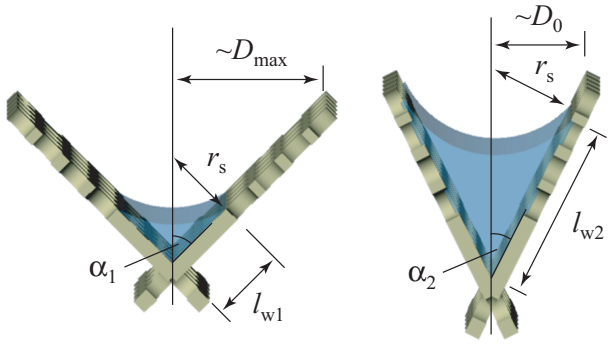

Figure 5.8: : Size change of the channel under hanging meniscus caused by the external pressure. Given the same radius of the surface curvature, r_s, two corners of different widths make different sized channels, which is directly associated with the local permeability.

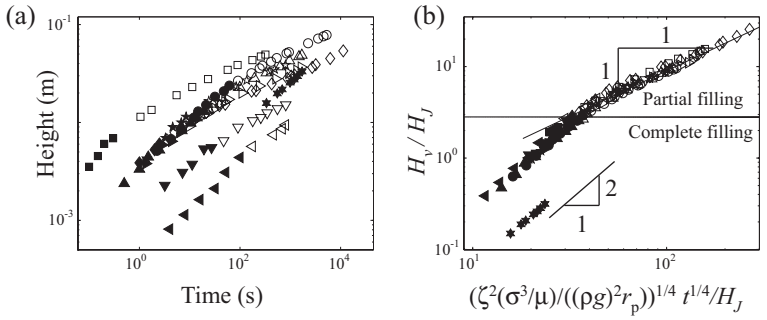

Figure 5.9: : Results of *partial filling* regime and boundary of the two regimes, *complete filling* and *partial filling*. (a) Plot of raw data points of vertical imbibition in early stage and late stage. (b) By employing the scaling analysis (5.4), the data points of vertical rise in late stage are coalesced onto one single line ($H_v \propto t^{1/4}$). Also, complete filling (early stage) and partial filling (late stage) are well separated by the Jurin's height of large voids.

Chapter 6

Concluding remarks

6.1 Conclusions

In this thesis, we have presented four different subjects, hydrodynamics of writing with ink, dynamics of hemiwicking, capillary rise between superhydrophilic substrates, and hydrodynamics of liquid imbibition in sponge. In all cases, parametric analysis and mathematical modeling have been performed to demonstrate the fundamental physics of each phenomena. For systematic approaches toward our final goal, hydrodynamics of capillary imbibition in porous media, stepwise researches have been performed in consecutive order.

In chapter 2, we introduced one of the most representative examples of capillary imbibition, ink absorbtion into paper. The study is performed by scaling analysis about the fundamental dynamics, associated with the spreading of a newtonian liquid on a porous substrate. Liquid spreading from stationary pen is addressed first, so that the basic dynamics of capillary spreading into fabric networks of the paper can be verified, by employing simplified model. After that the moving source rather than the stationary source has been addressed for analyzing the front profile and final thickness of the writing trace. We have considered geometric model

about moving source and volume conservation combining with the results from the stationary case.

In chapter 3, the superhydrophilic substrate employed as a model paper in chapter 2 is again used for more accurate theory. We have experimentally and theoretically studied capillary rise of a liquid deposited on a single substrate with micro pillar arrays. We have performed parametric analysis about especially characteristic of the pillar specification, such as diameter, height, and pitch. The theoretical approaches are performed with macroscopic and microscopic models in parallel. By the macroscopic model, we have constructed a scaling law showing excellent agreement with various pillar arrays. And by the microscopic model, we have found the validation limit of the scaling law derived from macroscopic model, starting from more fundamental level about the same phenomena. Meanwhile, the macroscopic scaling analysis that is widely used currently has been analyzed by the microscopic point of view.

In chapter 4, we introduced capillary imbibition in dual sized porous system, capillary rise within parallel superhydrophilic substrates. We have presented scaling laws for the bulk flow within the gap between the substrates and film flow through the micro pillar arrays partially associated with the bulk flow. Meanwhile, we have introduced general law of capillary rise between plates describing bulk rise and film rise simultaneously. Moreover, the film emanating height ahead of the bulk part has been investigated by comparing the bulk speed and the film initiating speed. Thus, the current work has quantitatively clarified the mechanism of the flow in dual porous media by accounting for the individual flows in large pore and small pore including the correlations.

In chapter 5, we have constructed the scaling laws to describe the dynamics of the horizontal and the vertical imbibition of different liquids into various cellulosic sponges, and corroborated the results using experiments. Unlike single sized porous media, multi-sized porous media, sponge, shows

different flow mechanics when against gravity, since the pores are selectively saturated by gravity, which gives an unusual result, $H_v \propto t^{1/4}$, different from the classical Washburn's rule, $L \propto t^{1/2}$. The imbibition is classified in two different flow types by whether entire pores are completely saturated or not, *complete filling* and *partial filling*.

Performing the researches above, we have mathematically formulated the fundamental physics of capillary phenomena. Our scaling laws are applicable for providing theoretical basis to related industrial fields, such as lab-on-a-chip, humidifier, heat pipe or other industries using porous media as a liquid channel. Furthermore, our experimental results and the scaling laws will contribute to future studies of liquid imbibition in porous media owing to the simplicity and high accuracy.

6.2 Future work

In this thesis, we have focused on systematical researches about capillary flow in porous media. In spite of our stepwise studies, there still remain many problems unanswered. Dynamics of corner flow between the porous plates is not yet been clarified. The phenomena involves imbibition in porous plate as well as normal flow within a corner of smooth sheets. The combination of the two phenomena is mundanely observed in nature and laboratory, but, at the same time, quite important to further delineate the dynamics of complex flow in general porous media. Moreover, swelling, elastocapillary effect, or chemical adhesion between liquids and substrates have not yet been studied. Those effects complicate the physics, thus, this subject should be further pursued in the future.

References

Bico, J., Thiele, U. & Quéré, D. (2002). Wetting of textured surfaces. *Colloids Surf., A*, **206**, 41–46.

Bird, J.C., Dhiman, R., Kwon, H.M. & Varanasi, K.K. (2013). Reducing the contact time of a bouncing drop. *Nature*, **503**, 385–388.

Butt, H.J., Craf, K. & Kappl, M. (2006). *Physics and chmistry of interfaces*. WILEY-VCH.

Conrath, M., Fries, N., Zhang, M. & Dreyer, M.E. (2010). Radial capillary transport from an infinte reservoir. *Transp. Porous Med.*, **84**, 109–132.

Courbin, L., Denieul, E., Dressaire, E., Roper, M., Ajdari, A. & Stone, H.A. (2007). Imbibition by polygonal spreading on microdecorated surfaces. *Nature Mat.*, **6**, 660–664.

Darcy, H. (1961). Les fontaines de la ville de dijon, victor dalmont. *Phil. Trans. Roy. Soc. London*, **57**, 1200–1207.

Davis, S.H. & Hocking, L.M. (2000). Spreading and imbibition of viscous liquid on a porous base. ii. *Phys. Fluids*, **12**, 1646–1655.

de Gennes, P.G., Brochard-Wyart, F. & Quéré, D. (2004). Capillarity and wetting phenomena.

Delker, T., Pengra, D.B. & Wong, P.Z. (1996). Interface pinning and dynamics of capillary rise in porous media. *Phys. Rev. Lett.*, **76**, 2902–2905.

Dong, M. & Chatzis, I. (1995). The imbibition and flow of a wetting liquid along the corners of a square capillary tube. *J. Colloid Interface Sci.*, **172**, 278–288.

Drechsler, A., Petong, N., Bellmann, C., Busch, P., Stamm, M., Grundke, K., Wunnicke, O. & Reichelt, J. (2010). Our measurement with a rheometer indicates that the ink shows a slightly shear-thickening behavior, that is, the viscosity increases with the shear rate. in our experiments, the shear rate is approximately (5 mm/s)/(5 μm)=100 s^{-1}, and the corresponding viscosity is 3.8 mpa·s.

Dreyer, M., Delgado, A. & Rath, H.J. (1994). Capillary rise of liquid between parallel plates under microgravity. *J. Colloid Interface Sci.*, **163**, 158–168.

Duarte, A.A., Strier, D.E. & Zanette, D.H. (1996). The rise of a liquid in a capillary tube revisited : A hydrodynamical approach. *Am. J. Phys.*, **64**, 413–418.

Fischer, S.R. (2005). *A History of Writing*. Reaktion, London.

Fuentes, J. & Cerro, R.L. (2005). Flow patterns and interfacial velocities near a moving contact line. *Experiments in Fluids*, **38**, 503–510.

Ishino, C., Reyssat, M., Reyssat, E., Okumura, K. & Quéré, D. (2007). Wicking within forests of micropillars. *Europhys. Lett.*, **79**, 56005.

Jurin, J. (1717-1719). An account of some experiments shown before the royal society; with an enquiry into the cause of the ascent and suspension of water in capillary tubes. *Phil. Trans.*, **30**, 739–747.

Kim, J., Moon, M.W., Lee, K.R., Mahadevan, L. & Kim, H.Y. (2011a). Hydrodynamics of writing with ink. *Phys. Rev. Lett.*, **107**, 264501.

Kim, J., Moon, M.W. & Kim, H.Y. (2015). Dynamics of hemiwicking. *Thesis*, **Chapter 2**.

Kim, S.J., Moon, M.W., Lee, K.R., Lee, D.Y., Chang, Y.S. & Kim, H.Y. (2011b). Liquid spreading on superhydrophilic miropillar arrays. *J. Fluid Mech.*, **680**, 477–487.

Kovacevic, R. (20125). *Welding processes*. InTech.

Lago, M. & Araujo, M. (2001). Capillary rise in porous media. *J. Colloid Interface Sci.*, **234**, 35–43.

Lee, A. & Kim, H.Y. (2014). Does liquid slippage within a rough channel always increase the flow rate? *Phys. Fluids*, **26**, 07002.

Levine, S., Lowndes, J., Watson, E.J. & Neale, G. (1979). A theory of capillary rise of a liquid in a vertical cylindrical tube and in a parallel-plate channel. *J. Colloid Interface Sci.*, **73**, 136–151.

Mahadevan, L. & Pomeau, Y. (1999). Rolling droplets. *Phys. Fluids*, **11**, 2449–2453.

Marmur, A. (1988). Penetration of a small drop into a capillary. *J. Colloid Interface Sci.*, **124**, 301–308.

Martinez, A.W., Phillips, S.T. & Whitesides, G.M. (2008). Three-dimensional microfluidic devices fabricated in layered paper and tape. *Proc Natl Acad Sci.*, **105**, 19606–19611.

Märtson, M., Viljanto, J., Hurme, T., Laippala, P. & Saukko, P. (1999). Is cellulose sponge degradable or stable as implantation material? an in vivo subcutaneous study in rat. *Biomaterials*, **20**, 1989–1995.

Millington, R.J. & Quirk, J.P. (1961). Permeability of porous solids. *Trans. Faraday Soc.*, **57**, 1200–1207.

Obara, N. & Okumura, K. (2012). Imbibition of a textured surface decorated by short pillars with rounded edges. *Phys. Rev. E.*, **86**, 020601.

Ponomarenko, A., Quéré, D. & Clanet, C. (2011). A universal law for capillary rise in corners. *J. Fluid Mech.*, **666**, 146–154.

Popescu, M.N., Ralston, J. & Sedev, R. (2008). Capillary rise with velocity-dependent dynamics contact angle. *Langmuir*, **24**, 12710–12716.

Quéré, D. (1997). Inertial capillarity. *Europhys. Lett.*, **39**, 533–538.

Richard, D. & Quéré, D. (1999). Viscous drops rolling on a tilted non-wettable solid. *Europhys. Lett.*, **48**, 286–291.

Srivastava, N., Din, C., Judson, A., MacDonald, N.C. & Meinhart, C.D. (2010). A. unified scaling model for flow through a lattice of microfabricated posts. *Lab Chip*, **10**, 1148–1152.

Tanner, L.H. (1979). The spreading of silicone oil drops on horizontal surfaces. *J. Phys. D*, **12**, 1473–1484.

Tsai, P., Pacheco, S., Pirat, C., Lefferts, L. & Kohse, D. (2009). Drop impact upon micro-nanostructured superhydrophobic surfaces. *Langmuir*, **25(20)**, 12293–12298.

Vella, D. & Huppert, H.E. (2007). The waterlogging of floating objects. *J. Fluid Mech.*, **585**, 245–254.

Washburn, E.W. (1921). The dynamics of capillary flow. *Phys. Rev.*, **17**, 273–283.

Weislogel, M.M. (2012). Compound capillary rise. *J. Fluid Mech.*, **709**, 622–647.

Wheeler, T.D. & Stroock, A.D. (2008). Transpiration of water at negative pressures in a synthetic tree. *Nature*, **455**, 208–212.

Xiao, R., Enright, R. & Wang, E.N. (2010). Prediction and optimization of liquid propagation in micropillar arrays. *Langmuir*, **26(19)**, 15070–15075.

Xiao, Y., Yang, F. & Pitchumani, R. (2006). A generalized analysis of capillary flows in channels. *J. Colloid Interface Sci.*, **298**, 880–888.

Yang, E. & Kim, H.Y. (2012). Junmping hoops. *Am. J. Phys.*, **80**, 19–23.

Yi, J.W., Moon, M.W., Ahmed, S.F., Kim, H., Cha, T.G., Kim, H.Y., Kim, S.S. & Lee, K.R. (2010). Long-lasting hydrophilicity on nanostructured si-incorporated diamon-like carbon films. *Langmuir*, **26**, 17203–17209.

Young, T. (1805). An essay on the cohesion of fluids. *Phil. Trans. Roy. Soc. London*, **95**, 65–87.

Zhmud, B.V., Tiberg, F. & Hallstensson, K. (2000). Dynamics of capillary rise. *J. Colloid Interface Sci.*, **228**, 263–269.

국 문 초 록

다공성 물질에서의 액체 흡수 역학

서울대학교 대학원
기계항공공학부
김 정 철

요 약

지구상의 대부분의 물질은 매끈한 표면 보다는 주로 작은 기공으로 이루어져 있다. 이 물질들이 특정 액체와 화학적으로 친밀한 성질을 가질 때, 해당 액체와 만나면 기공으로의 액체의 흡수 내지는 흡착이 이루어지게 된다. 액체의 표면 장력에 의해 일어나게 되는 이 액체의 흐름을 모세관 현상이라고 하는데, 우리 주위에서 매우 잘 관찰할 수 있다. 잉크가 종이에 퍼지는 것이나, 수건에 물이 흡수되는 현상 등이 대표적인 예이다. 이 현상은 산업계에서도 많이 응용되어 제습기, 가습기 산업 및 Lab on a chip 산업 등에서 직, 간접적으로 그 원리가 활용되고 있다. 그러나 이와 같은 다공성 물질에의 액체 흡수 메커니즘은 구조의 복잡성으로 인하여 매우 다양한 모세관 현상을 복합적으로 수반하고 있어 유동 해석이 난해하다. 본 연구에서는 다공성 물질에서의 액체 흡수 메커니즘 이해를 위하여 여러 단계적인 연구를 수행하였다.

우선 다공성 물질에의 액체 흡수 현상의 대표적인 현상인 글씨쓰

기의 물리학을 다루었다. 마이크로 스케일의 필라 어레이 및 유리관을 사용하여, 펜이 정지된 상태에서의 액체 퍼짐 원리를 실험적, 이론적으로 탐구하였고, 이 결과를 이용하여 펜이 일정한 속도로 이동할 때 액체 퍼짐에 대한 연구를 수행하였다. 우선 정지 상태에서의 액체 퍼짐에 대한 연구를 수행하였다. 퍼짐을 일으키는 표면장력과 이를 저지하는 전단응력을 비교하여 퍼짐의 속도 관계식을 도출하였다. 펜이 이동할 때에는 기하학적 분석을 추가로 수행하여 펜으로 선을 그을 때, 앞 부분의 퍼짐 형태를 예측하는 이론식을 도출하고, 이를 실험적으로 분석하였다. 뿐만 아니라 부피 보존식을 추가적으로 적용하여 퍼짐 두께를 예측하는 이론식을 도출, 검증하였다.

다음으로 앞선 연구에 사용된 마이크로 필라 어레이에의 액체 흡수에 대한 보다 심도 있는 연구를 수행하였다. 보다 다양한 마이크로 필라 표면에 적용할 수 있는 정확한 이론식을 도출하고, 실험으로 검증하였다. 본 연구를 통하여 표면 거칠기 뿐만 아니라 필라 간의 간격도 추가적으로 영향을 줄 수 있음을 보였다. 매크로 및 마이크로 스케일의 접근을 통하여 본 이론식의 적용 한계에 대한 분석을 수행하였고, 이 연구 분야에 널리 활용되고 있는 이론 분석에 대한 의미를 보다 세부적으로 알아 보았다.

본 연구에서는 앞서 언급한 단계 연구의 일환으로서 단일 스케일의 기공 구조가 아닌 다양한 크기의 기공 구조에 대한 연구도 수행하였다. 그 첫 번째 단계로 두 가지 크기의 기공구조에 대한 연구를 계획하고, 두 개의 평행하게 놓인, 마이크로 필라 어레이 표면 사이에서의 모세관 오름 현상에 대한 연구를 수행하였다. 밀리미터 간격의 두 판 사이의 bulk 유동과 마이크로 필라에서의 film 유동이 존

재한다. Bulk 유동이 우선 일어나고, 그 위에서 film 유동이 일어나는데, 두 가지 유동의 역학에 대해서 각각 이론식을 정립하고, 실험검증을 수행하였다. Bulk 유동이 일어날 때에는 주변의 마이크로 구조에 영향을 받지 않음을 확인할 수 있었다. Film 유동이 일어날 때에는 초기에는 bulk 에 영향을 받지만 나중에는 이와는 독립적인 유동이 일어나게 됨을 알 수 있었다. 뿐만 아니라 film 유동이 시작되는 시점 분석이나 그 직후의 유동 역학에 대한 연구를 수행하여 두 유동이 서로에게 미치는 영향도 분석하였다.

마지막으로 보다 실제적인 다공성 구조인 스폰지를 이용하여 액체 흡수 메커니즘을 분석하였다. 스폰지에는 매우 다양한 크기의 기공이 존재하는데, 이러한 구조에의 액체 유동을 이해하기 위해서 스폰지 구조에 대한 모델링을 수행하였다. 우선 중력의 영향을 배제시킨 수평 방향의 유동에 대한 연구를 수행하였고, 이 결과를 이용하여 수직 방향의 유동 연구를 수행하였다. 수직 방향 유동의 경우 밀리미터 사이즈의 큰 기공으로 인하여 초기 유동과 후기 유동이 서로 다른 메커니즘을 보임을 확인하였다. 모든 기공을 액체로 채우는 complete filling 과 부분적으로 채우는 partial filling 으로 나누어 설명하여 수평 및 수직 방향의 유동을 이론적 실험적으로 분석하였고, 퍼짐 거리가 시간의 1/2승에 비례하는 Washburn 법칙에서 벗어나 새로운 퍼짐 경향성인 시간의 1/4 승에 비례하는 법칙을 도출하였다. 시간의 1/2 승에 비례하는 유동은 complete filling 이 일어나서 유동을 일으키는 주된 기공의 사이즈와 유동을 저지하는 기공의 사이즈가 일정할 때 일어난다. 하지만 1/4 승에 비례하는 유동은 partial filling 이 일어나서 유동을 일으키는 포어의 크기는 매우 작아서 중력에 영향을 받지 않지만 유동을 저지시키는 포어의 크기는

중력에 의해 큰 포어에 부분적으로 채워진 액체 채널이 되로 때 일어 난다. 즉, 중력에 의하여 높이에 따라서 permeability 가 변하게 되어 이와 같은 결과가 일어나게 된다.

본 연구에서는 여러 다공성 표면에서의 액체 퍼짐에 대한 수학적, 실험적 연구를 수행하였다. 모든 연구에서 각 현상에 영향을 미치는 인자들에 대한 분석을 수행하였고, 이들을 수학적 모델링을 통하여 이론식에 반영하여 각 영향력을 구체화하였다. 따라서 본 연구 결과는 향후 학계나 산업계에서 해당 현상을 응용하고자 할 때, 이론적으로나 실험적 문제 해결에 큰 도움을 줄 것으로 예상한다.

주요어 : 표면장력, 다공성 구조, 모세관 현상, 초친수성 표면
학 번 : 2009 - 20672